

1 **Anatomical and physiological foundations of cerebello-hippocampal interactions**

2

3 **Authors:**

4 Watson TC^{1*}, Obiang P^{1*}, Torres-Herraez A^{1*}, Wattilliaux A¹, Coulon P², Rochefort C¹, Rondi-
5 Reig L^{1§}

6

7 **Affiliations:**

8 ¹ Neuroscience Paris Seine, Cerebellum, Navigation and Memory Team, CNRS UMR 8246;
9 INSERM, UMR-S 1130; Sorbonne Universités, University Pierre and Marie Curie, Paris,
10 France.

11 ² Institut de Neurosciences de la Timone, CNRS and Aix Marseille Université, 13385
12 Marseille cedex 05, France.

13

14 **Author Contributions:**

15 Designed the project and coordinated the grants and experiments

16 LRR

17 Designed experiments:

18 LRR, TCW, CR, PO, PC

19 Performed experiments:

20 PO, PC, TCW, ATH, AW

21 Designed analysis and analyzed data:

22 LRR, TCW, ATH, AW, PO

23 Wrote the paper:

24 LRR, TCW and ATH with comments from all the co-authors

25 * co-first authors

26

27 §To whom correspondence should be addressed. E-mail : laure.rondi-reig@upmc.fr IBPS-

28 Neurosciences Paris Seine, Sorbonne Université, UPMC Univ Paris 06, CeZaMe team, 9 Quai

29 Saint Bernard, 5e étage, 75005 Paris, France

30

31 **Conflict of Interest:** The authors declare no competing financial interests.

32

33 **Abstract**

34 Multiple lines of evidence suggest that functionally intact cerebello-hippocampal

35 interactions are required for appropriate spatial processing. However, how the cerebellum

36 anatomically and physiologically engages with the hippocampus to sustain such interactions

37 remains unknown. Using rabies virus as retrograde transneuronal tracer, we reveal that the

38 dorsal hippocampus receives input from topographically restricted and disparate regions of

39 the cerebellum. By simultaneously recording local field potential from both the dorsal

40 hippocampus and anatomically connected cerebellar regions, we additionally demonstrate

41 that the two structures interact, in a behaviorally dynamic manner, through subregion-

42 specific synchronization of neuronal oscillations in the 6-12Hz frequency range. Together,

43 these results reveal a novel neural network macro-architecture through which we can

44 understand how a brain region classically associated with motor control, the cerebellum,

45 may influence hippocampal neuronal activity and related functions, such as spatial

46 navigation.

47

48

49 **Introduction**

50 The cerebellum is classically associated with motor control. However, accumulating
51 evidence suggests its functions may extend to cognitive processes including navigation [1–
52 6]. Indeed, anatomical and functional connectivity has been described between cerebellum
53 and cortical areas that are engaged in cognitive tasks [7–12]. Furthermore, the cerebellum
54 has recently been found to form functional networks with subcortical structures associated
55 with higher-order functions, such as the basal ganglia [13], ventral tegmental area [14] and
56 hippocampus [15–18].

57 In the hippocampus, spontaneous local field potential (LFP) activity [19–22] and place cell
58 properties [23], are profoundly modulated following cerebellar manipulation [24 for
59 review]. A recent study has also described, at the single cell and blood-oxygen-level-
60 dependent signal level, sustained activation in the dorsal hippocampus during optogenetic
61 enhancement of cerebellar nuclei output in head-fixed mice [25]. These data point towards
62 the existence of an anatomical projection from the cerebellum to the hippocampus. The
63 suggestion of a direct connection between these two structures has been further supported
64 by a recent tractography study in humans [26] and the presence of short-latency evoked
65 field potentials (2-4 ms) in cat and rat hippocampi after electrical stimulation of the
66 cerebellar vermal and paravermal regions [27–31]. However, secondary hippocampal field
67 responses have also been described, at a latency of 12-15ms following cerebellar
68 stimulation, suggesting the existence of an indirect pathway [28].

69 Taken together, these studies provide compelling physiological evidence of cerebellar
70 influences on the hippocampus. Yet, they do not provide direct evidence of
71 neuroanatomical connectivity between the two regions. Given the known complex, modular
72 functional and anatomical organization of the cerebellum [32] this represents a major gap in

73 our understanding of the network architecture linking the two structures. What's more,
74 these studies provide no direct measure of physiological interactions between the regions,
75 which are thought to be essential for maintaining distributed network functions [e.g. 33].
76 Therefore, this study addresses two fundamental, unanswered questions: which regions of
77 the cerebellum are anatomically connected to the hippocampus and what are the spatio-
78 temporal dynamics of cerebello-hippocampal interactions during behavior? To address
79 these unresolved questions, we used rabies virus as a retrograde transneuronal tracer to
80 determine the extent and topographic organization of cerebellar input to the hippocampus.
81 Based upon the anatomical tracing results, we then studied interactions between the two
82 structures by simultaneously recording LFP from both the cerebellum and the dorsal
83 hippocampus in freely-moving mice. We reveal that specific cerebellar modules are
84 anatomically connected to the hippocampus and that these inter-connected regions
85 dynamically interact during behavior.

86

87 **Results**

88 To study the topographical organization of ascending, cerebello-hippocampal projections,
89 we unilaterally injected rabies virus (RABV), together with cholera toxin β -subunit (CTb),
90 into the left hippocampal dentate gyrus (DG). The use of CTb allowed us to identify and
91 measure the extent of the injection sites (Figure S1).

92 A precise topography of the cerebellum regions projecting to the hippocampus

93 We characterized the presence of retrograde transneuronally RABV-infected neurons after
94 survival times of 30, 48, 58 and 66 h [34,35]. Importantly, we did not find any RABV or CTb
95 labeling in the cerebellum at 30h post infection (p.i.), ruling out the existence of a direct
96 cerebello-hippocampal DG pathway in mice. Rather, RABV/CTb-labeled neurons were found

97 in two well described subcortical pathways leading to the DG of the hippocampus (first cycle
98 of infection). One labeled pathway included the diagonal band of Broca and the septum. The
99 other labeled hippocampal input pathway included the lateral entorhinal and perirhinal
100 cortices (Figure S2)[36–38]. At 48 h p.i., a few weakly RABV+/CTb- neurons were found in
101 contralateral deep cerebellar and vestibular nuclei (Fig. 1A, inset), likely reflecting the onset
102 of a second infection cycle. In agreement with this hypothesis, after 58 h p.i., i.e. inside the
103 12 h time window required for completion of a viral replication cycle [39] we found robust
104 RABV labeling bilaterally in fastigial, dentate and vestibular nuclei, and a small number of
105 weakly labeled neurons in the posterior nucleus interpositus (Fig. 1B-F). At 58 h p.i. we also
106 observed few labeled cells in the cerebellar cortex (Fig. 1A, inset), suggesting the beginning
107 of an overlapping, third infection cycle. Within the two most labeled cerebellar nuclei,
108 fastigial and dentate, RABV-labeled cells were found to be topographically restricted to
109 caudal and central regions, respectively (Fig. 1G).

110 -----FIGURE 1 NEAR HERE-----

111 Following 66 h of incubation, the number of strongly labeled cells increased in the DCN and
112 vestibular nuclei (Fig. 1 A); however, the topographical distribution remained unchanged
113 (Fig. S3). At the level of the cerebellar cortex, longitudinal clusters of RABV+ Purkinje cells
114 (PCs) were found in a bilateral manner across highly restricted central and flocculo-nodular
115 regions (Fig. 1L). The bilateral cerebellar patterning of RV labeled cells observed after
116 unilateral hippocampal injections likely reflects the existence of commissural connections
117 within the pathway rather than the existence of bilateral projections arising from the
118 cerebellum. The presence of labeling in the contralateral hippocampus at the earliest
119 survival time (30h; Table 1) and the appearance at 48h of RV labeled neurons exclusively in
120 the contralateral cerebellar output nuclei are consistent with this hypothesis. In the central

121 cerebellum, clusters were particularly concentrated in lobule VI and Crus I (Fig. 1 H, I, M). In
122 the flocculo-nodular cerebellum, RABV-labeled cells were found in the dorsal and ventral
123 paraflocculus (Fig. 1 J and M and Fig. 2B). Within the vermis we identified a single cluster of
124 RABV+ Purkinje cells that extended across both lobule VIa and lobule VIb-c (Fig. 2). In
125 contrast, within Crus I, RABV-labeled Purkinje cells were arranged in two spatially isolated
126 clusters, one located rostro-laterally and the other caudo-medially (Fig. 2).

127 The topographical arrangement of RABV-labeled PCs in longitudinal clusters is in keeping
128 with the well-described modular organization of the cerebellum [e.g. 32]. Mapping of
129 molecular marker expression patterns, such as zebrin II banding, provides a reliable basis
130 from which modules can be defined and recognized in the cerebellar cortex of rodents.
131 Thus, to further assign the observed PC clusters to previously described cerebellar zones, we
132 used a double immunohistochemical approach to stain for both RABV and aldolase C (zebrin
133 II) in one animal (case S18) 66 h after infection (Fig. 2B) [40,41]. Lobule VI, Crus I and
134 paraflocculus are mostly zebrin positive regions [42] and we found that RABV-labeled
135 Purkinje cells co-localized with zebrin II in all the observed clusters (Fig. 2B). In the vermis,
136 lobule VIa RABV-labeled PCs were mostly located in the a+ band. The few RABV-labeled cells
137 found in lobule VII were confined to the 2+ band. Thus, together, these labeled cells belong
138 to the a+//2+ pair that constitutes part of the cerebellar A module (Fig. 2C) [43]. In Crus I,
139 the rostrolateral cluster of RABV-labeled PCs was aligned with the anterior 6+ zebrin band
140 corresponding to module D2. The caudomedial cluster was in continuation with the
141 posterior 5+ zebrin band suggesting that it is part of the paravermal module C2 (Fig. 2C). In
142 the paraflocculus, the assignment of the RABV-labeled cells to specific modules was not
143 addressed given the complex morphology of this region. However, the presence of RABV-

144 labeled cells both in the dorsal and ventral paraflocculus suggests the involvement of more
145 than one module (Fig. 2B-C) [44].

146 Cerebellar modules are also defined by their outputs through the deep cerebellar and
147 vestibular nuclei [32,45]. The presence of RABV-labeled cells in the fastigial nucleus is
148 consistent with the involvement of module A. Similarly, the D2 module is routed through
149 the dentate nuclei in which we find robust RABV labeling. We also found RABV+ cells in the
150 nucleus interpositus posterior, which provides the output of module C2. Finally, RABV
151 labeling was observed in the vestibular nuclei, which may represent the output of RABV+
152 Purkinje cells clusters observed in the ventral paraflocculus. Together, our neuroanatomical
153 tracing data indicate that cerebellar projections to the hippocampus emanate from three
154 distinct cerebellar modules subserving diverse functions.

155 -----FIGURE 2 NEAR HERE-----

156

157 Cerebello-hippocampal physiological interactions in a familiar home-cage environment

158 In order to question the potential functional relevance of cerebello-hippocampal anatomical
159 connectivity, we implanted mice (n = 21) with arrays of bipolar LFP recording electrodes in
160 bilateral dorsal hippocampus (HPC) and unilaterally in two highly RABV-labeled regions of
161 the central cerebellum, lobule VI (midline) and Crus I (left hemisphere). For comparison, we
162 also simultaneously recorded LFP from cerebellar regions with minimal RABV labeling
163 (lobule II or lobule III; Fig. 1M; Fig. 3A and B). Data were excluded from further analysis in
164 cases where postmortem histological inspection revealed that electrode positions were off-
165 target Fig. S4).

166 The spectral profile of cerebellar and hippocampal LFP activity was first assessed during
167 active movement in a familiar home-cage environment (see methods; mean speed, 2.7 ± 0.3
168 cm/s). Within the HPC, a dominant 6-12Hz theta oscillation was similarly observed in both
169 hemispheres (Fig. S5B; left HPC: peak spectral frequency = 7.81 ± 0.13 Hz, mean 6-12Hz z-
170 score power = 1.54 ± 0.07 , N = 17 mice; right HPC: peak spectral frequency = 7.72 ± 0.12 Hz,
171 mean 6-12Hz z-score power = 1.54 ± 0.07 , N = 19 mice; unpaired t test, $t_{34} = 0.007$, $p = 0.99$).
172 Fig. 3C shows combined spectra from both left and right HPC peak spectral frequency = 7.76
173 ± 0.09 Hz, mean 6-12Hz z-score power = 1.55 ± 0.05).

174 Although a clear peak in the 6-12 Hz band was not detected in cerebellar recordings,
175 transient 6-12 Hz oscillations were recorded (Fig. 3C and S6). The mean 6-12 Hz z-score
176 power did not differ between the different cerebellar recording sites (Fig. 3C; Crus I: $0.80 \pm$
177 0.30 , N = 13 mice; lobule II/III: 0.84 ± 0.03 , N = 11 mice; lobule VI: 0.79 ± 0.02 , N = 19 mice;
178 one-way ANOVA, $F_{(2, 40)} = 0.85$, $p = 0.43$).

179 As an indicator of cross-structure interaction [33], we next calculated coherence between
180 LFP recorded from the different cerebellar subregions and left or right HPC. We found no
181 statistically significant influence of hippocampal laterality on cerebello-hippocampal
182 coherence (Fig. S5C-E hemisphere x combination two-way ANOVA, hemisphere effect $F_{(1, 69)}$
183 $= 0.23$, $p = 0.64$, interaction effect, $F_{(2, 69)} = 0.06$, $p = 0.94$). Therefore, for further analysis, we
184 grouped these coherence values.

185 A single peak in coherence was observed for all cerebello-hippocampal combinations in the
186 theta frequency range (6-12 Hz, Fig. 3D; Crus I-HPC peak coherence = 7.99 ± 0.13 Hz, lobule
187 II/III-HPC peak coherence = 8.75 ± 0.16 Hz, lobule VI-HPC peak coherence = 8.55 ± 0.11 Hz).
188 However, significant differences across combinations were observed within this bandwidth
189 and LFP oscillations were significantly more synchronised between HPC and lobule VI than

190 with lobule II/III (Fig. 3D and E; mean lobule VI-HPC coherence, 0.245 ± 0.006 ; mean lobule
191 II/III-HPC coherence, 0.223 ± 0.004 ; Kruskal-Wallis with FDR correction, $q = 0.045$; lobule VI,
192 $n = 33$ values/20 mice; lobule II/III, $n = 19$ values/11 mice). Within lobule VI, coherence was
193 significantly correlated to the mediolateral position of the recording electrode, which was
194 consistent with the mediolateral location of greatest RABV-labeled PCs (Fig. 3F; linear
195 regression, $R^2 = 0.35$, $F_{(1, 27)} = 14.45$, $p = 0.0007$). Mean coherence between HPC and Crus I
196 (0.24 ± 0.01 ; $n = 23$ values/13 mice) was not significantly higher than with lobule II/III (Fig.
197 3E; Kruskal-Wallis with FDR correction, $q > 0.05$).

198 -----FIGURE 3 NEAR HERE-----

199 Cerebello-hippocampal interactions during the learning of a goal-directed behavior

200 To further characterize the dynamics of cerebello-hippocampal interactions, we quantified
201 cerebello-hippocampal theta coherence during a goal-directed task. A subset of mice ($n=8$)
202 were trained to traverse a linear track to get a reward (medial forebrain bundle stimulation,
203 see methods) at a fixed position (Fig. 4A).

204 Across training, mice improved their performance as shown by the optimisation of their
205 path (Fig. 4A), significant increase in the number of rewards obtained per trial (Fig. 4B;
206 mean number of rewards obtained on 1st trial = 16 ± 3 , mean number of rewards obtained
207 on 20th trial = 81 ± 15 ; one-way repeated measures ANOVA, $F_{(2.882, 20.18)} = 8.93$, $p < 0.001$)
208 and the significant increase in their mean speed (Fig. 4B; mean speed on 1st trial = $6.61 \pm$
209 0.30 cm/s, mean speed on 20th trial = 13.86 ± 1.56 cm/s; one-way repeated measures
210 ANOVA, $F_{(2.45, 17.15)} = 5.631$, $p = 0.0098$). Thus, we next explored the dynamics of LFP power
211 and cerebello-hippocampal 6-12Hz coherence across this learning period.

212 In the hippocampus, theta oscillations remained dominant in the recorded LFP throughout
213 training. A significant increase in both the mean theta power (Fig. 4C, S7A) and the peak
214 frequency (Fig. S7B) was observed in parallel with the performance and this was
215 independent of the hippocampal hemisphere (theta power: trial effect $F_{(19, 209)} = 3.11$, $p <$
216 0.0001 , hemisphere effect $F_{(1, 11)} = 0.30$, $p = 0.60$; interaction effect, $F_{(19, 209)} = 1.14$, $p = 0.31$;
217 peak frequency: trial effect, $F_{(19, 209)} = 8.84$, $p < 0.0001$, hemisphere effect $F_{(1, 11)} = 0.73$, $p =$
218 0.41 , interaction effect $F_{(19, 209)} = 0.16$, $p > 0.99$). In accordance with this finding, post-hoc
219 analysis revealed that mean theta power and peak frequency were significantly different
220 between first and last trials (Fig. 4E-F; mean z-score HPC theta power; mean on 1st trial =
221 1.64 ± 0.05 , mean on 20th trial = 1.72 ± 0.04 , $q = 0.0180$; peak frequency, mean trial 1 = 8.02
222 ± 0.15 Hz, mean trial 20 = 8.26 ± 0.13 Hz, $q = 0.0205$).

223 In the cerebellum, a global variation in the mean theta power was observed across trials but
224 no difference was found between Crus I, lobule VI and lobule II/III and no significant
225 variation was found between the last and first trials (Fig. 4C; Crus I: mean trial 1 theta power
226 = 0.73 ± 0.05 , mean trial 20 theta power = 0.71 ± 0.03 , $N = 5$ mice; lobule II/III: mean trial 1
227 LFP power = 0.86 ± 0.03 , mean trial 20 theta power = 0.87 ± 0.07 , $N = 6$ mice; lobule VI:
228 mean trial 1 theta power = 0.78 ± 0.03 , mean trial 20 theta power = 0.77 ± 0.06 , $N = 7$ mice;
229 cerebellar region x trial two-way repeated measures ANOVA with FDR correction, cerebellar
230 region effect, $F_{(2, 15)} = 2.88$, $p = 0.09$, trial effect $F_{(19, 285)} = 3.08$, $p < 0.0001$, interaction effect
231 $F_{(38, 285)} = 0.72$, $p = 0.89$, no trial was different from trial 1).

232 However, as learning progressed, cerebello-hippocampal theta coherence evolved in a non-
233 uniform manner (Fig. 4D; trial x combination two-way repeated measures ANOVA, trial
234 effect $F_{(19, 494)} = 2.42$, $p < 0.001$, combination effect $F_{(2, 26)} = 4.09$, $p = 0.028$, interaction
235 effect $F_{(38, 494)} = 3.43$, $p < 0.0001$). Post-hoc analysis revealed that only Crus I-HPC coherence

236 increased significantly across trials compared to initial values (multiple comparisons against
237 trial 1 with FDR correction; $q < 0.05$ for trials 5 and 7-20; Fig. 4D) and this was independent
238 of hippocampal hemisphere (Fig. S7C). Furthermore, this increase resulted in changes in the
239 differences in coherence observed between cerebello-hippocampal recording combinations.
240 Indeed, while during initial trials no significant inter-regional differences were observed, in
241 later trials, Crus I became significantly more coherent with HPC than lobule II/III and lobule
242 VI (Fig. 4D, multiple comparisons between combinations with FDR correction; Crus I vs
243 lobule II/III $q < 0.05$ for trials 5 and 8-20; Crus I vs lobule VI $q < 0.05$ for trials 8-12 and 14-
244 20). Unlike the observed shift in peak frequency of HPC theta power across trials, the peak
245 frequency of theta coherence remained constant for all the cerebello-hippocampal
246 combinations (Fig. S7D; Crus I-HPC: mean peak frequency = 8.41 ± 0.09 Hz, hemisphere x
247 trial two-way ANOVA, hemisphere effect, $F_{(1, 6)} = 0.98$, $p = 0.36$, trial effect $F_{(19, 114)} = 1.17$, p
248 = 0.30, interaction effect $F_{(19, 114)} = 0.48$, $p = 0.97$; lobule II/III-HPC: 9.08 ± 0.09 Hz,
249 hemisphere x trial two-way ANOVA, hemisphere effect, $F_{(1, 7)} = 1.59$, $p = 0.25$, trial effect,
250 $F_{(19, 133)} = 1.33$, $p = 0.18$, interaction effect, $F_{(19, 133)} = 0.97$, $p = 0.50$; lobule VI-HPC: mean
251 peak frequency = 8.78 ± 0.05 Hz, hemisphere x trial two-way ANOVA, hemisphere effect, $F_{(1,$
252 $10)} = 0.15$, $p = 0.70$, trial effect, $F_{(19, 190)} = 1.21$, $p = 0.25$, interaction effect, $F_{(19, 190)} = 0.53$, $p =$
253 0.94). Further examination of the power and coherence spectra across a wider frequency
254 range (1 to 45 Hz) in trials 1 and 20 confirmed that the observed changes across training
255 were restricted to the theta band (Fig. 4 E-H).

256 -----FIGURE 4 NEAR HERE -----

257 To examine whether the observed changes in coherence across learning of the linear track
258 were specifically related to performance of the goal-directed task itself, we next conducted
259 pairwise analysis of cerebello-hippocampal theta coherence levels across the following

260 conditions: home-cage prior to any linear track training (HC pre LT), first and last trials in the
261 linear track (early and late LT), and home-cage following the end of training in the linear
262 track task (HC post LT).

263 From the three cerebello-hippocampal recording configurations, only Crus I-HPC 6-12Hz
264 coherence varied significantly across task conditions (Fig. 5, Crus I-HPC: Friedman test with
265 FDR correction, Friedman statistic = 15.45, $p = 0.0015$). At the outset of linear track learning,
266 HPC-Crus I coherence values did not significantly differ from home-cage (HC pre LT = $0.25 \pm$
267 0.02 ; early LT = 0.26 ± 0.02 ; HC pre LT vs early LT $q = 0.44$). However, during late stage linear
268 track learning, the level of coherence was significantly higher than in home-cage recordings
269 and early stages of learning (late LT = 0.29 ± 0.03 ; HC pre LT vs late LT $q = 0.0015$; early LT vs
270 late LT $q = 0.0016$). When mice were returned to the home-cage environment following
271 completion of linear track training (HC post LT) the level of HPC-Crus I coherence dropped
272 significantly, back to pre-training levels (HC post LT = 0.26 ± 0.02 ; late LT vs HC post LT $q =$
273 0.012). We further analyzed changes in running speed and 6-12Hz power across conditions
274 and found that their pattern of modulation was markedly different from the observed Crus
275 I-HPC theta coherence dynamics (Fig. S8 and Fig. 5). While speed significantly varied
276 between all conditions, 6-12 Hz power remained stable in both in the HPC and cerebellar
277 recordings (Fig. S8). Together this suggests that the observed coherence dynamics appear to
278 be at least partially independent of changes in speed or 6-12Hz oscillation power.

279 -----FIGURE 5 NEAR HERE-----

280

281 Cerebello-hippocampal interactions during locomotion in a virtual environment

282 Our data indicate the presence of dynamic coherence between distinct cerebellar lobules
283 and the dorsal hippocampus during goal-directed behavior. To investigate if this interaction

284 requires the presence of specific sensory inputs, we further analyzed cerebello-hippocampal
285 6-12Hz coherence under conditions in which such inputs are not relevant for the behavioral
286 task.

287 Head fixed mice were trained to locate rewards (medial forebrain bundle stimulation) at
288 fixed positions on a virtual-reality based linear track (VR; Fig. 6A and B; see Methods). In this
289 paradigm, vestibular, olfactory and whisker information cannot be reliably used to learn the
290 task and thus it is likely that behavioral performance is linked mainly to visuo-motor
291 information processing. Mice rapidly reached a stable performance level as illustrated by a
292 stable running speed and number of rewards obtained (Fig. 6C) (mean speed: trial 4 = $7.61 \pm$
293 1.50 cm/s, trial 21 = 8.76 ± 2.78 cm/s, one-way repeated measures ANOVA, $F_{(1.789, 8.945)} =$
294 0.82 , $p = 0.82$; mean number of rewards: trial 4 = 25 ± 5 , trial 21 = 36 ± 16 , one-way
295 repeated measures ANOVA, $F_{(1.519, 7.596)} = 0.93$, $p = 0.41$; $N = 6$ mice). Although HPC theta
296 peak frequency was variable across trials with stable behavioral performance (trials 4 to 21,
297 Fig. S9A), mean 6-12Hz power and coherence values were similar (Fig. S9B-C) and therefore
298 collapsed across these trials for further analysis (Fig. 6D-F)

299 In keeping with results obtained in home-cage and real world (RW) linear track experiments,
300 coherence spectra calculated between either Crus I, lobule VI or lobule II/III and HPC
301 contained a single peak in the 6-12Hz theta frequency range (Fig. 6E). In this condition, 6-
302 12Hz coherence levels between HPC and both Crus I and lobule VI were again significantly
303 higher in comparison to lobule II/III (Fig. 6F; Kruskal-Wallis with FDR correction, $H = 10.93$,
304 Crus I-HPC vs lobule II/III-HPC $q = 0.0021$, lobule VI vs lobule II/III $q = 0.0077$, Crus I vs lobule
305 VI $q = 0.2998$; Crus I $n = 5$, lobule VI $n = 9$, lobule II/III $n = 8$).

306 -----FIGURE 6 NEAR HERE-----

307

308 In an effort to isolate the impact of changing sensory information on observed cerebello-
309 hippocampal interactions from the influence of ongoing motor behavior, we next made
310 pairwise comparisons of theta coherence values from recordings made during RW and VR
311 linear track tasks in specific trials in which the number of rewards obtained and mean
312 running speed was similar in both conditions (Fig. 7A; number of rewards: LT = 37 ± 4 , VR =
313 36 ± 4 , paired t test, $t_5 = 0.54$, $p = 0.46$; speed: LT = 8.36 ± 0.47 cm/s, VR = 8.50 ± 0.56 cm/s,
314 paired t test $t_5 = 0.68$, $p = 0.67$; N = 6 mice). Patterns of coherence in the selected RW trials
315 resembled those observed during late training in the LT (Fig. 7B; differences in mean 6-12 Hz
316 coherence: one way ANOVA with FDR correction $F_{(2, 19)} = 4.55$, Crus I-HPC vs lobule II/III $q =$
317 0.015 , Crus I-HPC vs lobule VI-HPC $q = 0.048$, lobule VI-HPC vs lobule II/III-HPC $q = 0.21$;
318 compare with Fig. 4H) and the selected VR trials closely mirrored the overall, pooled data
319 (Fig. 7C; Kruskal-Wallis with FDR correction, $H = 9.02$, Crus I-HPC vs lobule II/III $q = 0.009$,
320 Crus I-HPC vs lobule VI-HPC $q = 0.33$, lobule VI-HPC vs lobule II/III-HPC $q = 0.007$; compare
321 with Fig. 6E), respectively. In these epochs of comparable motor state, Crus I-HPC coherence
322 was reduced significantly in the VR condition compared to RW (Fig. 7D; RW = $0.2974 \pm$
323 0.030 , VR = 0.2721 ± 0.022 ; paired t test $T_4 = 2.82$, $p = 0.047$; $n = 5$). In contrast, lobule VI
324 and lobule II/III – hippocampal coherence was similar across conditions (Fig. 7D; lobule VI:
325 RW = 0.250 ± 0.011 , VR = 0.260 ± 0.014 , paired t test $T_7 = 1.63$, $p = 0.39$, $n = 9$; lobule II/III:
326 RW = 0.239 ± 0.008 , VR = 0.216 ± 0.002 , paired t test, $T_8 = 0.86$ $p = 0.18$, $n = 8$).

327 -----FIGURE 7 NEAR HERE-----

328

329 **Discussion**

330

331 Taken together, our findings reveal previously undescribed cerebellar inputs to the
332 hippocampus and offer novel physiological insights into a long-range neural network linking
333 disparate brain regions initially assumed to support divergent behavioral functions, namely
334 spatial navigation (hippocampus) and motor control (cerebellum). Topographically
335 restricted regions of cerebellar cortex discretely route through restricted parts of their
336 associated nuclei en-route to the hippocampus. Congruently, our physiological data reveal
337 that these connected cerebellar regions dynamically interact with the hippocampus during
338 behavior, via 6-12 Hz LFP coherence. Our findings thus offer an anatomical and physiological
339 framework for cerebello-hippocampal interactions that could support cerebellar
340 contributions to hippocampal processes [3], including spatial map maintenance [17,23,24].

341 Whilst previous studies provide compelling physiological evidence of cerebellar influences
342 on the hippocampus [19–22,25,46], they do not provide the spatial resolution afforded by
343 neuroanatomical tracing. Indeed, to the best of our knowledge, anatomical tracing studies
344 have failed to report a mono-synaptic ascending cerebello-hippocampal projection. This is
345 consistent with our rabies virus tracing study, in which incubation periods of 48-58 h were
346 required before cell labeling was seen in the cerebellar nuclei. Such a timescale is indicative
347 of a multi-synaptic pathway [35,47–49] potentially involving indirect connectivity through
348 the forebrain navigation circuits.

349 Our anatomical results highlight three main inputs to the hippocampus emanating from the
350 cerebellum. The first input we reveal originates from the vestibulo-cerebellum, specifically
351 from the dorsal and ventral paraflocculus, which is likely routed via the vestibular and
352 dentate nuclei [44]. This anatomical connection between the vestibulo-cerebellum and the

353 hippocampus reinforces the already well described influence of the vestibular system on
354 hippocampal dependent functions [50–52].

355 In addition to the classically described vestibular pathway, our data reveal that the central
356 cerebellum also provides inputs to the hippocampus from vermal lobule VI, routed through
357 caudal fastigial nucleus, and from Crus I, routed through the dentate. Using a combination
358 of RABV expression and zebrin II staining we identified three specific cerebellar modules
359 involved in these inputs: (1) the A module in lobule VI, (2) the hemispheric Crus I D2 module
360 and (3) the Crus I paravermal C2 module. Of the latter two modules, C2 is likely less
361 prominently anatomically connected with the hippocampus since the number of RABV+ cells
362 in the nucleus interpositus posterior, its output nucleus [32], was minor compared with the
363 other cerebellar nuclei. The convergence of inputs from disparate cerebellar zones (flocculo-
364 nodular and central zones) and modules from vermal (A), paravermal (C2) and hemispheric
365 (D2) regions in to the hippocampus suggest that its optimal function requires the integration
366 of multiple aspects of sensory-motor processing carried out at these distinct cerebellar
367 locations.

368 The A module in lobule VI is part of the so-called oculomotor vermis. It receives climbing
369 fibers from the caudal medial accessory olive, and sends mainly ascending projections
370 through the caudal portion of fastigial nucleus [53]. The oculomotor vermis receives
371 multiple sensory inputs which include visual, proprioceptive, vibrissae, vestibular and
372 auditory inputs conveyed by both climbing and mossy fibers [44]. It projects to, amongst
373 others, the superior colliculus and other visual structures of the midbrain, the vestibular
374 nuclei, the periaqueductal grey and the ventro-medial nucleus of the thalamus [54].
375 Notably, all of these regions contained RABV+ cells at 48h p.i., and thus they cannot be
376 excluded as potential routes towards the hippocampus. The D2 module receives its climbing

377 fiber input from the dorsal cap of the principal olive and projects out of the cerebellum
378 through the rostromedial dentate nucleus [55]. It receives mossy fiber inputs carrying
379 somatosensory, motor [56], and visual [57] information; along with inputs from the
380 prefrontal cortex [7]. Climbing fiber inputs to this module relay information from the
381 parvocellular red nucleus, which receives projections from premotor, motor, supplementary
382 motor and posterior parietal areas. The majority of these cortical areas also receive
383 projections from the D2 module after a thalamic relay in the ventro-lateral nucleus [7,58].

384 Complementary to these anatomical results, our electrophysiological findings reveal
385 coherent activity between the hippocampus and those cerebellar lobules that are
386 anatomically connected with it (lobule 6 and Crus I). This interaction was restricted to the 6-
387 12 Hz range in the awake, behaving animal and showed non-uniform, dynamic profiles that
388 were lobule dependent. Oscillations can align neuronal activity within and across brain
389 regions, facilitating cross-structure interactions [e.g 33,59]. Cerebellar circuits support
390 oscillations across a range of frequencies [for review see 60,61]. Of particular relevance to
391 the current study are reports of oscillations within the theta frequency (~4-12 Hz), which
392 have been described in the cerebellar input layers at the Golgi [62] and granule cell [e.g.
393 63,64] level, and also in the cerebellar output nuclei [9,65]. Indeed, despite of the absence
394 of prominent sustained theta band activity in our overall cerebellar recordings, we could
395 record transient 6-12 Hz cerebellar oscillations (Fig S6).

396 Neuronal coherence has been described across the cerebro-cerebellar system at a variety of
397 low frequencies [9,66–71] and oscillations within the theta range are thought to support
398 inter-region communication across a wide variety of brain regions [72]. Our finding that
399 cerebello-hippocampal coherence is limited to the 6-12 Hz bandwidth is in keeping with
400 previous studies on cerebro-cerebellar communication in which neuronal synchronization

401 has been observed between the cerebellum and prefrontal cortex [9,67], primary motor
402 cortex [66,70], supplementary motor area [66] and sensory cortex [66]. Furthermore, local
403 field potentials recorded in the hippocampus and cerebellar cortex are synchronized within
404 the theta bandwidth during trace eye-blink conditioning in rabbits [73]. Human brain
405 imaging studies have also described co-activation of blood oxygen level dependent signals in
406 both cerebellar and hippocampal regions during navigation [15] and spatio-temporal
407 prediction tasks [74], thus highlighting neuronal putative interactions between the two
408 structures. Regarding studies in mice, a recent study has demonstrated the existence of
409 statistically significant co-activation of the dorsal hippocampus and cerebellar lobules IV-V,
410 lobule VI and Crus I after the acquisition of a sequence-based navigation task [16].

411 Multiple lines of evidence suggest that the phase-locking described here is unlikely to have
412 resulted from volume conduction: 1) Rather than using a common reference electrode, our
413 recordings were bipolar, with each recording electrode being locally and independently
414 referenced [75]. 2) If volume conduction of theta oscillations was emanating from a
415 hippocampal source then it could be assumed that cerebellar regions in closer proximity to
416 the hippocampus would show higher levels of coherence (Fig. S5A). However, we found that
417 coherence values were not related to the relative distance between the hippocampus and
418 cerebellar recording site. 3) Hippocampal theta power increased over training in our linear
419 track paradigm, whereas 6-12 Hz power remained stable across all cerebellar recording
420 sites. However, significant coherence was only observed between hippocampus and Crus I.
421 Thus, the observed coherence was unlikely to have resulted from co-variation in theta
422 power between the two areas.

423 Importantly, we have shown for the first time that theta rhythms in the hippocampus
424 preferentially phase lock with those in discrete regions of the cerebellum and that degree of

425 this coupling changes depending upon the behavioral context. Lobule VI-hippocampus
426 coherence was dominant during active movement in the home-cage and remained stable
427 during learning of the real world linear track task. On the other hand, Crus I-HPC coherence
428 was highly dynamic, showing a significant increase over the learning of the real world linear
429 track task and becoming dominant after the acquisition of a goal-directed behavior.
430 Interestingly, although multiple streams of sensory input, including those of a vestibular,
431 whisker and olfactory nature, become irrelevant and even confounding in the head-
432 restricted virtual environment task, Crus I-HPC and lobule VI-HPC coherence remained high
433 in this condition. Paired-comparisons of trial epochs containing similar behavioural
434 performances in the real-world and virtual environment revealed that Crus I-HPC coherence
435 is significantly reduced in the latter while no change was observed for lobule VI-HPC.

436 We next consider our results within the modular understanding of cerebellar function.
437 Within lobule VI, the A module receives multi-modal sensory information, mainly arising
438 from collicular and vestibular centres [44]. The superior colliculus plays a role in visual
439 processing and generation of orienting behaviors [76], which might be relevant for the
440 establishment and maintenance of the hippocampal spatial map, and thus may be required
441 constantly during active movement, independent of the specific behavioral task. The
442 persistent and similar levels of lobule VI-HPC coherence during active movement in the
443 homecage and linear track task, in both real world and virtual reality environment tasks is in
444 agreement with such a hypothesis.

445 In monkeys and humans, Crus I is anatomically and functionally associated with prefrontal
446 cortex [7,15]. In rat Crus I, the D2 module receives convergent sensory and motor
447 information [77]. Furthermore, this module has been found to contain internal models, a
448 neural representation of one's body and the external world based on memory of previous

449 experiences, that are used for visuo-motor coordination [78]. Similarly, the C2 module has
450 been found to also participate in visuo-motor processing related to limb coordination during
451 goal-directed reaching [79]. Both modules might be particularly important during the
452 acquisition of a goal-directed behavior such as our real-world linear track task in which
453 animals needed to reach non-cued reward zones. Our finding that Crus I-HPC coherence
454 increases during task learning fits with this hypothesis. Furthermore, the observed reduction
455 of Crus I-HPC coherence levels in the head-restricted, virtual environment task may reflect
456 the reduced recruitment of cerebellar modules that are involved in processing of non-
457 relevant sensory modalities, since only visuo-motor information can be reliably used to
458 learn the task.

459 In summary, our results suggest the existence of both, an anatomically discrete
460 hippocampal-cerebellar network interactions and a topographical dynamic weighting of
461 these interactions potentially tailored to the prevailing sensory context and behavioral
462 demands.

463

464

465 **Methods**

466 Anatomical tracing studies were performed under_protocol N°00895.01, in agreement with
467 the Ministère de l'Enseignement Supérieur et de la Recherche. RABV injections were
468 performed by vaccinated personnel in a biosafety containment level 2 laboratory.

469 All behavioral experiments were performed in accordance with the official European
470 guidelines for the care and use of laboratory animals (86/609/EEC) and in accordance with
471 the Policies of the French Committee of Ethics (Decrees n° 87–848 and n° 2001–464). The
472 animal housing facility of the laboratory where experiments were made is fully accredited
473 by the French Direction of Veterinary Services (B-75-05-24, 18 May 2010). Surgeries and
474 experiments were authorized by the French Direction of Veterinary Services (authorization
475 number: 75-752).

476 A total of 39 adult, male mice were used for this study. 18 adult male C57BL6-J mice were
477 used for the anatomical tracing study, (Charles River, France) and 21 for the
478 electrophysiology study (Janvier, France). 3 adult male CD-L7ChR2 mice were used for the
479 dual hippocampal LFP and cerebellar unit-recording study (in-house colony derived from
480 Jackson labs stock, USA).

481 Mice received food and water *ad libitum*, were housed individually (08: 00–20: 00 light
482 cycle) following surgery and given a minimum of 5 days post-surgery recovery before
483 experiments commenced.

484 **1. Anatomy**

485 **Rabies virus injections**

486 All the RABV (the French subtype of Challenge Virus Standard; CVS-N2C) inoculations were
487 performed in the Plasticity and Physio-Pathology of Rhythmic Motor Networks (P3M)
488 laboratory, Timone Neuroscience Institute, Marseille, France. Mice (n= 18) were injected
489 intraperitoneally with an anesthetic mixture of ketamine (65 mg/kg; Imalgene, France) and
490 xylazine (12 mg/kg; Rompun, Bayer) to achieve surgical levels of anesthesia, as evidenced by
491 the absence of limb withdrawal and corneal reflexes and lack of whisking and were then
492 placed in a stereotaxic frame (David Kopf Instruments, USA). The scalp was then incised, the
493 skull exposed and a craniotomy drilled above the hippocampus.

494 Mice were injected with 200 nL of a mixture of one part 1% CTb Alexa Fluor® 488 Conjugate
495 (Invitrogen, distributed by Life Technologies, Saint Aubain, France) and four parts RABV in
496 the left hippocampus (AP -2.0, ML +2.0, DV 1.97; Fig. 1, Fig. S1). Injections (200 nL/min)
497 were performed using a pipette connected to a 10 µL Hamilton syringe mounted on a
498 microdrive pump. Following infusion, the pipette was left in place for 5 min. The incision
499 was then sutured and the animals allowed to recover in their individual home cage for
500 either 30h (n= 5); 48 h (n= 3), 58h (n= 5) or 66 h (n=5). All animals were carefully monitored
501 during the survival period and, in line with previous studies using these survival times, were
502 found to be asymptomatic [48].

503 **Tissue preparation**

504 At the end of the survival time, mice were deeply anesthetized with sodium pentobarbitone
505 (100mg/kg, intraperitoneal) then transcardially perfused with 0.9 % saline solution
506 (15mL/min) followed by 75 mL of 0.1M phosphate buffer (PB) containing 4 %
507 paraformaldehyde (PFA; pH = 7.4). The brain was then removed, post fixed for 2-3 days in 4
508 % PFA and then stored at 4°C in 0.1 M PB with 0.02% sodium azide. Extracted brains were
509 then embedded in 3 % agarose before being coronally sectioned (40 µm) on a vibratome.

510 Serial sections were collected and divided in 4 vials containing 0.1 M PB so consecutive
511 slices in each vial were spaced 160 μm .

512 **Injection site visualization**

513 Sections from vial 1 were used to visualize the injection site by the presence of CTb. In most
514 of the cases, the injected CTb was fluorescent and sections were directly mounted with Dapi
515 Fluoromount G (SouthernBiotech®, Alabama, USA). In the other cases (S4-5, S11-13 and
516 S17-18), the sections were first rinsed with PB 0.1M and then permeated with PB 0.1 M and
517 0.3 % Triton X-100. They were then incubated overnight in a choleraenoid antibody raised
518 in goat (goat anti-CTb, lot no. 703, List Biological Laboratories, USA) diluted 1: 2000 in a
519 blocking solution (PB 0.1 M, 5 % BSA). Subsequently, the sections were rinsed in PB 0.1M
520 and incubated 4 h at room temperature with donkey anti-goat secondary antibody (1: 1000
521 in the blocking solution; Alexa Fluor® 555, Invitrogen, distributed by ThermoFisher Scientific,
522 Massachusetts, USA). Finally, they were also mounted with Dapi Fluoromount G.

523 The injection site was then visualized using a fluorescence microscope equipped with a
524 fluorescein isothiocyanate filter (Axio Zoom V16, Carl Zeiss, France).

525

526 **Rabies virus labeled cell quantification**

527 Sections from vial 2 were used for quantification and 3 D reconstruction of the RABV labeled
528 cells. Sections mounted on gelatin-coated SuperFrost®Plus slides (Menzel-Glaser,
529 Braunschweig, Germany) were first rinsed with PB 0.1 M and pre-treated with 3 % H_2O_2
530 during 30 minutes for blocking reaction against endogenous peroxidase. Following
531 pretreatment, the sections were incubated overnight at room temperature with an anti-
532 rabies phosphoprotein mouse monoclonal antibody [80] diluted at 1: 10000 in a blocking

533 solution (PB 0.1 M, 0.1 % BSA, goat serum 2 % and 0.2 % Triton X-100). The day after, the
534 sections were rinsed in PB 0.1M and incubated 2 hours with a biotinylated affinity-purified
535 goat anti-mouse IgG (1: 2000 in blocking solution; Santa-Cruz, Heidelberg, Germany). Then,
536 they were also incubated using an avidin-biotin complex method (Vectastain Elite ABC-
537 Peroxidase kit R.T.U. Universal, Vector Laboratories, Burlingame, CA, USA) to enhance
538 sensitivity. For visualization, the sections were incubated in a 3,3'-diaminobenzidine-
539 tetrahydrochloride (DAB) solution (0.05 % DAB and 0.015 % H₂O₂ in PB 0.1 M). Finally, they
540 were counterstained with Cresyl and cover-slipped.

541 Quantitative analyses of rabies-positive nuclei were performed using a computerized image
542 processing system (Mercator, Exploranova, France) coupled to an optical microscope. The
543 quantification of rabies-positive nuclei was carried out at 10x magnification. Structures were
544 defined according to a standard atlas [81]. Immunoreactive neurons were counted
545 bilaterally. Representative images were obtained using an Axio Zoom V16 microscope (Carl
546 Zeiss, France).

547 **3-D reconstruction**

548 A Nikon Eclipse E800 microscope equipped with a digital color camera (Optronics, USA) was
549 used to visualize mounted cerebellar sections under brightfield illumination. The contour of
550 every 4th section was then manually drawn using Microfire software (Neurolucida, MBF
551 Bioscience, USA) and cell counts were performed. The sections were then aligned and
552 stacked (160 µm spacing).

553 **Rabies virus-zebrin II double immuno-staining**

554 For case S18, sections from vial 3 were mounted on gelatin-coated SuperFrost[®]Plus slides
555 (Menzel-Glaser, Braunschweig, Germany), rinsed with PB 0.1M and then permeated and

556 blocked in a solution of PB 0.1 M, 0.2 % Triton X-100 and bovine serum 2.5% for 30 minutes.
557 Then they were incubated during 48h at 4°C in a mix of rabbit polyclonal anti-Aldolase C
558 primary antibody (a kind gift from Izumi Sugihara [41]; No. 69075; 1:500000) and the mouse
559 anti-rabies antibody used for the single RABV staining (1:5000) in a blocking solution (PB 0.1
560 M, 0.1 % Triton X-100 and bovine serum 1 %). Subsequently, the sections were first rinsed
561 with PB 0.1 % and then incubated in a mix of RRX-Goat anti-rabbit IgG (1: 5000; ref 111-295-
562 144, Jackson Immuno Research) and donkey anti-mouse secondary antibody (1: 5000; Alexa
563 Fluor® 647, Invitrogen distributed by ThermoFisher Scientific, Massachusetts, USA) in
564 blocking solution. Finally, they were also mounted with Dapi Fluoromount G.
565 Images were obtained using an Axiozoom v16 microscope (Carl Zeiss, France) and contour
566 and labeled neurons in the cerebellum were manually draw for reconstruction of the zebrin
567 bands and cerebellar modules and location of the RABV+ cells.

568 **2. Electrophysiology procedures**

569 **Subjects and surgical protocols**

570 Bipolar LFP recording electrodes (interpolar distance of ~0.5mm; 140µm diameter Teflon
571 coated stainless-steel, A-M system, USA) were stereotaxically targeted to hippocampus (AP -
572 2.2, ML +2.0, DV 1.0), lobule 6 (AP -6.72, ML 0.0, DV 0.1), lobule 2 (AP -5.52, ML 0.0, DV 1.8)
573 and Crus I (AP -6.24, ML 2.5, DV 0.1) of 21 C57BL6-J mice. Pairs of flexible stainless-steel
574 wires were used to also record neck EMG (Cooner wire, USA)

575 In 15 C57BL6-J mice, bipolar stimulation electrodes (140-µm-diameter stainless steel; A-M
576 system, USA) were also implanted at the left medial forebrain bundle [MFB; to serve as a
577 reward signal; AP -1.4, ML +1.2, DV +4.8 [Cf. 82,83]. All electrode assemblies were fixed to
578 the skull using a combination of UV activated cement (SpeedCem, Henry Shein, UK),

579 SuperBond (SunMedical, Japan) and dental cement (Simplex Rapid, Kemdent, UK). Four
580 miniature screws (Antrin, USA) were also attached to the skull for additional support and to
581 serve as recording ground.

582 In 6 mice, a lightweight metal head fixation device (0.1g) was also implanted. The total
583 implant weight did not exceed 2.5g (including head fixation post and cement).

584 **Recording**

585 Signals from all electrodes were attached to an electronic interface board (EIB 18,
586 Neuralynx, USA) either during surgery. Differential recordings were made via a unity-gain
587 headstage preamplifier (HS-18; Neuralynx, USA) and Digital Lynx SX acquisition system
588 (Neuralynx, USA). LFP and EMG Signals were bandpass-filtered between 0.1 and 600 Hz and
589 sampled at 1 kHz. Mouse position was tracked at 30Hz using video tracker software and
590 infra-red LEDs attached to the headstage (Neuralynx, USA).

591 **MFB Stimulation**

592 Intracranial rewarding stimulation consisted of a 140Hz stimulation train lasting 100ms
593 delivered through the headstage to the implanted electrodes (SD9k, Grass Technologies,
594 USA). Optimal voltage for intracranial MFB was determined for each mouse with a nose-
595 poke task prior to training (range, 1-6V [Cf. 82]).

596 **Histology**

597 After completion of all the experiments, mice were deeply anesthetized with
598 ketamine/xylazine solution (150mg/kg) and electrolytic lesions created by passing a positive
599 current through the electrodes (30 μ A, 10sec). With the electrodes left *in situ*, the animals
600 were perfused transcardially with saline followed by paraformaldehyde (4%).

601 Brains were extracted and post-fixed in paraformaldehyde (4%; 24h) then embedded in
602 agarose (24h). A freezing vibratome was used to cut 50 μ m thick sagittal cerebellar and

603 coronal hippocampal sections. The sections were mounted on gelatinised slides and stained
604 with cresyl violet. Recording locations were identified by localised lesions in the cerebellum
605 and hippocampus and plotted on standard maps with reference to a stereotaxic atlas [81].

606 **3. Behavioral procedures**

607 **Familiar environment**

608 All recordings were made in the animal's home-cage (30 cm x 10 cm x 10 cm plastic box),
609 with the lid removed and lasted a maximum of 4 hours. Recordings were made during the
610 day between the hours of 10 am to 18:00 pm.

611 **Linear track – real world**

612 The linear track was made in-house from 100 cm x 4 cm x 0.5 cm of black plastic positioned
613 20cm above the surface of the experimental table. The behavioral assembly was located in a
614 separate room from the experimenter and was surrounded on four sides by black curtains.
615 Three salient visual cues were placed at fixed locations along the edge of the track (10 cm
616 from the edge). Mice were trained to run in a sequential manner from one end of the track
617 to the other in order to receive a reward, which consisted of an electrical stimulation of the
618 MFB. The reward stimulation was delivered automatically when the mice reached a 5 cm
619 wide goal-zone, which was located 10 cm from the end of the track. Timing of the reward
620 signal was logged on the electrophysiological recordings via TTL signals. Sessions lasted 12
621 mins and were repeated 3 times per day with an inter-session time of 5 mins over 7 days.
622 Between sessions, the track was cleaned with 20 percent ethanol.

623 **Linear track – virtual reality environment**

624 A commercially available virtual-reality environment was used (Jet Ball, Phenosys,
625 Germany), utilising an air cushioned Styrofoam ball (200 mm), which served as a spherical
626 treadmill for head restrained mice [Cf. 84] (Supplementary Fig. 12). The floating ball
627 assembly was positioned 20 cm from a series of six octagonally arranged TFT surround
628 monitors (19 inch) such that the head restrained mice had an unobstructed view of the

629 visual scene. Rotation of the Styrofoam ball was detected by an optical sensor (sampling
630 frequency 5700 dots per inch at 1 kHz). The vertical axis signals were interpreted by the VR
631 software as the forward and backward movement of the virtual position of the animal.
632 Position within the VR was then translated to a voltage signal (zero to five volts, with 5 volts
633 indicating the end of the track), and sent to the Digital Lynx SX (Neuralynx, USA)
634 electrophysiology system via a DACQ interface (DACQ 6501, National Instruments, USA). The
635 start of the VR display was logged on the electrophysiology recordings via a TTL signal. To
636 provide a reward signal, when the mice reached a given location within the VR (10 cm from
637 the end of the track) a TTL marker was sent to both the electrophysiological recording
638 system (to provide a timestamp-marker of the event) and an electrical stimulus generator
639 linked to the HS-18 headstage (in the same manner as for RW linear track experiments).
640 The virtual scene consisted of a 1 m long track with grey walls and included 3 salient visual
641 cues. After 3 x 12 mins sessions of habituation to the head fixation on the floating-ball
642 assembly, mice were trained to run on the linear track in 12 min sessions, 3 times per day
643 with an inter-session interval of approximately 5 mins during 7 days. The number of rewards
644 received by the animal was logged in the electrophysiology software (Cheetah 5.6.3,
645 Neuralynx, USA).

646 **Behavioral and electrophysiological analysis**

647 All data were processed in_Matlab (Mathworks, USA), Spike 2 (Cambridge Electronic
648 Design, UK) and Prism (Graphpad, USA).

649 **1. Behavior**

650 In the home-cage environment, behavioral data were selected using a custom-made Matlab
651 script. Interactive cursors were used to define periods of active movement, based upon
652 speed (derived from video tracking data), EMG and LFP signals. For the purpose of further
653 analysis, we focused on periods of active movement (indicated by high EMG amplitude,
654 speed and hippocampal 6-12 Hz oscillations). The overall mean speed of each mouse was
655 then calculated across all the selected data epochs.

656 For RW linear track experiments, in each 12 minute trial (3 trials per day) the number of
657 rewards (indicated by TTL markers), distance traveled, speed and an efficiency score
658 (distance traveled per reward) were calculated using a custom Matlab script. These
659 parameters were calculated on a trial-by-trial basis (from trial 2 onwards).

660 In virtual reality-based experiments, for each 12min trial (3 trials per day), the number of
661 rewards (timestamped by TTL markers) and virtual speed was calculated using a custom
662 Matlab script. Virtual speed was calculated using the virtual environment X and Y coordinate
663 values (recorded as voltage signals in Neuralynx Cheetah software).

664 **2. Electrophysiology**

665 Multi-taper Fourier analyses (Chronux toolbox [85]) were used to calculate power and
666 coherence of the LFP data. We used a 10s sliding window (9s overlap) and 19 tapers for all
667 analysis, except for the example presented in Fig. S6 in which we used a 2s sliding window
668 (1.5s overlap) and 3 tapers. Statistical comparison was restricted to the 6-12 Hz frequency
669 band unless otherwise stated.

670 For recordings made in the home-cage environment, LFP data were manually selected, as
671 described above for behavioral data. Analysis was focused on LFP gathered during periods
672 of active movement. Selected data were then filtered to remove any large-amplitude, low
673 frequency artifacts using a stationary wavelet transform [86]. Spectral power and coherence
674 were then calculated. The spectral power between 0.1 and 45 Hz was z-scored due to inter-
675 animal variations in LFP magnitude. Mean power and coherence were calculated in the 6-
676 12Hz frequency range for all cerebello-hippocampal combinations. Data duration in the
677 home-cage environment varied across mice (range, 12 to 132 min). Therefore, to reduce the
678 impact of data length on subsequent analyses and also to match with subsequent linear
679 track experiments (duration of 12 min), for each mouse we concatenated the LFP in to 12
680 min blocks. When multiple 12 min blocks were available (number of data blocks ranged
681 from 1 to 11) we calculated the average coherence across all blocks. The number of 12
682 minute blocks used was found to have no correlation with the overall level of calculated
683 coherence (See Fig. S5F).

684 For RW and virtual linear track recordings, general electrophysiological analysis methods
685 were the same as described for home-cage recordings including artifact removal procedures
686 (in this case MFB stimulation artifacts were also removed using the methodology described
687 in [86]). In addition to pooled calculations (in which analysis was conducted across all trials

688 of the task), power and coherence was also calculated on a trial-by-trial basis across
689 learning.

690 **Statistical analysis**

691 Statistical analyses were conducted using Matlab Statistical Toolbox and Prism (Graphpad,
692 USA). Normality was assessed using a Shapiro-Wilk test. Parametric and non-parametric
693 tests were then used accordingly.

694

695 **Acknowledgements**

696 This work was supported by the Fondation pour la Recherche Médicale DEQ20160334907-
697 France, by the National Agency for Research ANR-17-CE16-0019-03 (LRR), by the CNRS and
698 Aix-Marseille Université through UMR 7289 (PC). This work also received support under the
699 program Investissements d'Avenir launched by the French Government and implemented
700 by the ANR, with the references, PER-SU (LRR) and ANR-10-LABX-BioPsy (LRR). The group of
701 LRR is member of the Labex BioPsy and ENP Foundation. Labex are supported by French
702 State funds managed by the ANR within the Investissements d'Avenir programme under
703 reference ANR-11-IDEX-0004-02. We thank Roxanna Ureta for help with histology, Lilith
704 Sommer for help with behavioral experiments, Gregory Sedes and Nadine Francis for help
705 developing analysis codes, and Richard Apps for his insightful comments. We are grateful to
706 Richard Hawkes and Izumi Sugihara for generously providing the aldolase C antibody.
707 Finally, we thank all members of the CEZAME team for helpful discussions of the
708 experiments and manuscript.

709

710

711

712 **References**

- 713 1. Petrosini L, Leggio MG, Molinari M. The cerebellum in the spatial problem solving: a co-star
714 or a guest star? *Prog Neurobiol.* 1998;56: 191–210. Available:
715 <http://www.ncbi.nlm.nih.gov/pubmed/9760701>
- 716 2. Rondi-Reig L, Burguière E. Is the cerebellum ready for navigation? *Progress in brain research.*
717 2005. pp. 199–212. doi:10.1016/S0079-6123(04)48017-0
- 718 3. Burguière E, Arleo A, Hojjati M reza, Elgersma Y, Zeeuw CI De, Berthoz A, et al. Spatial
719 navigation impairment in mice lacking cerebellar LTD: a motor adaptation deficit? *Nat*
720 *Neurosci.* 2005;8: 1292–1294. doi:10.1038/nn1532
- 721 4. Koziol LF, Budding D, Andreasen N, D’Arrigo S, Bulgheroni S, Imamizu H, et al. Consensus
722 Paper: The Cerebellum’s Role in Movement and Cognition. *The Cerebellum.* 2014;13: 151–
723 177. doi:10.1007/s12311-013-0511-x
- 724 5. Buckner RL. The Cerebellum and Cognitive Function: 25 Years of Insight from Anatomy and
725 Neuroimaging. *Neuron.* 2013;80: 807–815. doi:10.1016/j.neuron.2013.10.044
- 726 6. Stoodley CJ, D’Mello AM, Ellegood J, Jakkamsetti V, Liu P, Nebel MB, et al. Altered cerebellar
727 connectivity in autism and cerebellar-mediated rescue of autism-related behaviors in mice.
728 *Nat Neurosci.* 2017;20: 1744–1751. doi:10.1038/s41593-017-0004-1
- 729 7. Kelly RM, Strick PL. Cerebellar loops with motor cortex and prefrontal cortex of a nonhuman
730 primate. *J Neurosci.* 2003;23: 8432–44. Available:
731 <http://www.ncbi.nlm.nih.gov/pubmed/12968006>
- 732 8. Ramnani N. The primate cortico-cerebellar system: anatomy and function. *Nat Rev Neurosci.*
733 Nature Publishing Group; 2006;7: 511–522. doi:10.1038/nrn1953
- 734 9. Watson TC, Becker N, Apps R, Jones MW. Back to front: cerebellar connections and
735 interactions with the prefrontal cortex. *Front Syst Neurosci.* 2014;8: 4.

- 736 doi:10.3389/fnsys.2014.00004
- 737 10. Watson TC, Jones MW, Apps R. Electrophysiological mapping of novel prefrontal - cerebellar
738 pathways. *Front Integr Neurosci.* 2009;3: 18. doi:10.3389/neuro.07.018.2009
- 739 11. Stoodley CJ, Schmahmann JD. Evidence for topographic organization in the cerebellum of
740 motor control versus cognitive and affective processing. *Cortex.* 2010;46: 831–844.
741 doi:10.1016/j.cortex.2009.11.008
- 742 12. Kim SG, Uğurbil K, Strick PL. Activation of a cerebellar output nucleus during cognitive
743 processing. *Science.* 1994;265: 949–51. Available:
744 <http://www.ncbi.nlm.nih.gov/pubmed/8052851>
- 745 13. Chen CH, Fremont R, Arteaga-Bracho EE, Khodakhah K. Short latency cerebellar modulation
746 of the basal ganglia. *Nat Neurosci.* 2014;17: 1767–75. doi:10.1038/nn.3868
- 747 14. Rogers TD, Dickson PE, Heck DH, Goldowitz D, Mittleman G, Blaha CD. Connecting the dots of
748 the cerebro-cerebellar role in cognitive function: Neuronal pathways for cerebellar
749 modulation of dopamine release in the prefrontal cortex. *Synapse.* 2011;65: 1204–1212.
750 doi:10.1002/syn.20960
- 751 15. Iglói K, Doeller CF, Paradis A-L, Benchenane K, Berthoz A, Burgess N, et al. Interaction
752 Between Hippocampus and Cerebellum Crus I in Sequence-Based but not Place-Based
753 Navigation. *Cereb Cortex.* 2015;25: 4146–4154. doi:10.1093/cercor/bhu132
- 754 16. Babayan BM, Watilliaux A, Viejo G, Paradis A-L, Girard B, Rondi-Reig L. A hippocampo-
755 cerebellar centred network for the learning and execution of sequence-based navigation. *Sci*
756 *Rep.* 2017;7: 17812. doi:10.1038/s41598-017-18004-7
- 757 17. Rochefort C, Lefort J, Rondi-Reig L. The cerebellum: a new key structure in the navigation
758 system. *Front Neural Circuits.* 2013;7: 35. doi:10.3389/fncir.2013.00035
- 759 18. Yu W, Krook-Magnuson E. Cognitive Collaborations: Bidirectional Functional Connectivity

- 760 Between the Cerebellum and the Hippocampus. *Front Syst Neurosci.* 2015;9: 177.
761 doi:10.3389/fnsys.2015.00177
- 762 19. Iwata K, Snider R. Cerebello-hippocampal influences on the electroencephalogram.
763 Electroencephalogr Clin Neurophysiol. 1959;11: 439–46. Available:
764 <http://www.ncbi.nlm.nih.gov/pubmed/13663818>
- 765 20. Babb TL, Mitchell AG, Crandall PH. Fastigiobulbar and dentatohalamic influences on
766 hippocampal cobalt epilepsy in the cat. *Electroencephalogr Clin Neurophysiol.* 1974;36: 141–
767 154. doi:10.1016/0013-4694(74)90151-5
- 768 21. Snider RS, Maiti A. Septal afterdischarges and their modification by the cerebellum. *Exp*
769 *Neurol.* 1975;49: 529–39. Available: <http://www.ncbi.nlm.nih.gov/pubmed/811491>
- 770 22. Krook-Magnuson E, Szabo GG, Armstrong C, Oijala M, Soltesz I. Cerebellar Directed
771 Optogenetic Intervention Inhibits Spontaneous Hippocampal Seizures in a Mouse Model of
772 Temporal Lobe Epilepsy. *eNeuro. Society for Neuroscience*; 2014;1.
773 doi:10.1523/ENEURO.0005-14.2014
- 774 23. Rocheffort C, Arabo A, Andre M, Poucet B, Save E, Rondi-Reig L. Cerebellum Shapes
775 Hippocampal Spatial Code. *Science (80-)*. 2011;334: 385–389. doi:10.1126/science.1207403
- 776 24. Rondi-Reig L, Paradis A-L, Lefort JM, Babayan BM, Tobin C. How the cerebellum may monitor
777 sensory information for spatial representation. *Front Syst Neurosci.* 2014;8: 205.
778 doi:10.3389/fnsys.2014.00205
- 779 25. Choe KY, Sanchez CF, Harris NG, Otis TS, Mathews PJ. Optogenetic fMRI and
780 electrophysiological identification of region-specific connectivity between the cerebellar
781 cortex and forebrain. *Neuroimage.* 2018;173: 370–383.
782 doi:10.1016/j.neuroimage.2018.02.047
- 783 26. Arrigo A, Mormina E, Anastasi GP, Gaeta M, Calamuneri A, Quartarone A, et al. Constrained

- 784 spherical deconvolution analysis of the limbic network in human, with emphasis on a direct
785 cerebello-limbic pathway. *Front Hum Neurosci.* 2014;8: 987. doi:10.3389/fnhum.2014.00987
- 786 27. Newman PP, Reza H. Functional relationships between the hippocampus and the cerebellum:
787 an electrophysiological study of the cat. *J Physiol.* 1979;287: 405–26. Available:
788 <http://www.ncbi.nlm.nih.gov/pubmed/430426>
- 789 28. Whiteside J, Snider R. Relation of cerebellum to upper brain stem. *J Neurophysiol.* 1953;16:
790 397–413. Available: <http://www.ncbi.nlm.nih.gov/pubmed/13070051>
- 791 29. Snider RS, Maiti A. Cerebellar contributions to the papez circuit. *J Neurosci Res.* 1976;2: 133–
792 146. doi:10.1002/jnr.490020204
- 793 30. Harper JW, Heath RG. Anatomic connections of the fastigial nucleus to the rostral forebrain in
794 the cat. *Exp Neurol.* 1973;39: 285–92. Available:
795 <http://www.ncbi.nlm.nih.gov/pubmed/4573973>
- 796 31. Heath RG, Dempsey CW, Fontana CJ, Myers WA. Cerebellar stimulation: effects on septal
797 region, hippocampus, and amygdala of cats and rats. *Biol Psychiatry.* 1978;13: 501–29.
798 Available: <http://www.ncbi.nlm.nih.gov/pubmed/728506>
- 799 32. Apps R, Hawkes R. Cerebellar cortical organization: a one-map hypothesis. *Nat Rev Neurosci.*
800 2009;10: 670–81. doi:10.1038/nrn2698
- 801 33. Fries P. A mechanism for cognitive dynamics: neuronal communication through neuronal
802 coherence. *Trends Cogn Sci.* 2005;9: 474–480. doi:10.1016/j.tics.2005.08.011
- 803 34. Aoki S, Coulon P, Ruigrok TJH. Multizonal Cerebellar Influence Over Sensorimotor Areas of
804 the Rat Cerebral Cortex. *Cereb Cortex.* 2017; doi:10.1093/cercor/bhx343
- 805 35. Suzuki L, Coulon P, Sabel-Goedknecht EH, Ruigrok TJH. Organization of cerebral projections to
806 identified cerebellar zones in the posterior cerebellum of the rat. *J Neurosci.* 2012;32: 10854–
807 69. doi:10.1523/JNEUROSCI.0857-12.2012

- 808 36. Mosko S, Lynch G, Cotman CW. The distribution of septal projections to the hippocampus of
809 the rat. *J Comp Neurol.* 1973;152: 163–174. doi:10.1002/cne.901520204
- 810 37. Dolorfo CL, Amaral DG. Entorhinal cortex of the rat: topographic organization of the cells of
811 origin of the perforant path projection to the dentate gyrus. *J Comp Neurol.* 1998;398: 25–48.
812 Available: <http://www.ncbi.nlm.nih.gov/pubmed/9703026>
- 813 38. Witter MP. The perforant path: projections from the entorhinal cortex to the dentate gyrus.
814 *Progress in brain research.* 2007. pp. 43–61. doi:10.1016/S0079-6123(07)63003-9
- 815 39. Coulon P, Bras H, Vinay L. Characterization of last-order premotor interneurons by
816 transneuronal tracing with rabies virus in the neonatal mouse spinal cord. *J Comp Neurol.*
817 2011;519: 3470–3487. doi:10.1002/cne.22717
- 818 40. Brochu G, Maler L, Hawkes R. Zebrin II: a polypeptide antigen expressed selectively by
819 Purkinje cells reveals compartments in rat and fish cerebellum. *J Comp Neurol.* 1990;291:
820 538–52. doi:10.1002/cne.902910405
- 821 41. Sugihara I, Shinoda Y. Molecular, topographic, and functional organization of the cerebellar
822 cortex: a study with combined aldolase C and olivocerebellar labeling. *J Neurosci.* 2004;24:
823 8771–85. doi:10.1523/JNEUROSCI.1961-04.2004
- 824 42. Sugihara I, Quy PN. Identification of aldolase C compartments in the mouse cerebellar cortex
825 by olivocerebellar labeling. *J Comp Neurol.* 2007;500: 1076–92. doi:10.1002/cne.21219
- 826 43. Sugihara I. Compartmentalization of the Deep Cerebellar Nuclei Based on Afferent
827 Projections and Aldolase C Expression. *The Cerebellum.* 2011;10: 449–463.
828 doi:10.1007/s12311-010-0226-1
- 829 44. Voogd J, Barmack NH. Oculomotor cerebellum. *Progress in brain research.* 2006. pp. 231–
830 268. doi:10.1016/S0079-6123(05)51008-2
- 831 45. Ruigrok TJH. Ins and outs of cerebellar modules. *Cerebellum.* 2011;10: 464–74.

- 832 doi:10.1007/s12311-010-0164-y
- 833 46. Cooke P, Snider R. Some cerebellar influences on electrically-induced cerebral seizures.
834 Epilepsia. 1955;4: 19–28. Available: <http://www.ncbi.nlm.nih.gov/pubmed/13305547>
- 835 47. Jwair S, Coulon P, Ruigrok TJH. Disynaptic Subthalamic Input to the Posterior Cerebellum in
836 Rat. Front Neuroanat. Frontiers; 2017;11: 13. doi:10.3389/fnana.2017.00013
- 837 48. Ugolini G. Advances in viral transneuronal tracing. J Neurosci Methods. 2010;194: 2–20.
838 doi:10.1016/j.jneumeth.2009.12.001
- 839 49. Kelly RM, Strick PL. Rabies as a transneuronal tracer of circuits in the central nervous system.
840 J Neurosci Methods. 2000;103: 63–71. doi:10.1016/S0165-0270(00)00296-X
- 841 50. Zheng Y, Goddard M, Darlington CL, Smith PF. Long-term deficits on a foraging task after
842 bilateral vestibular deafferentation in rats. Hippocampus. 2009;19: 480–6.
843 doi:10.1002/hipo.20533
- 844 51. Goddard M, Zheng Y, Darlington CL, Smith PF. Locomotor and exploratory behavior in the rat
845 following bilateral vestibular deafferentation. Behav Neurosci. 2008;122: 448–59.
846 doi:10.1037/0735-7044.122.2.448
- 847 52. Stackman RW, Clark AS, Taube JS. Hippocampal spatial representations require vestibular
848 input. Hippocampus. 2002;12: 291–303. doi:10.1002/hipo.1112
- 849 53. Akaike T. The tectorecipient zone in the inferior olivary nucleus in the rat. J Comp Neurol.
850 1992;320: 398–414. doi:10.1002/cne.903200311
- 851 54. Teune TM, van der Burg J, van der Moer J, Voogd J, Ruigrok TJH. Topography of cerebellar
852 nuclear projections to the brain stem in the rat. Progress in brain research. 2000. pp. 141–
853 172. doi:10.1016/S0079-6123(00)24014-4
- 854 55. Herrero L, Yu M, Walker F, Armstrong DM, Apps R. Olivo-cortico-nuclear localizations within
855 crus I of the cerebellum. J Comp Neurol. 2006;497: 287–308. doi:10.1002/cne.20976

- 856 56. Mihailoff GA, Burne RA, Azizi SA, Norell G, Woodward DJ. The pontocerebellar system in the
857 rat: An HRP study. II. Hemispherical components. *J Comp Neurol.* 1981;197: 559–577.
858 doi:10.1002/cne.901970403
- 859 57. Edge AL, Marple-Horvat DE, Apps R. Lateral cerebellum: functional localization within crus I
860 and correspondence to cortical zones. *Eur J Neurosci.* 2003;18: 1468–85. Available:
861 <http://www.ncbi.nlm.nih.gov/pubmed/14511327>
- 862 58. Glickstein M, Sultan F, Voogd J. Functional localization in the cerebellum. *Cortex.* 2011;47:
863 59–80. doi:10.1016/j.cortex.2009.09.001
- 864 59. Singer W. Neuronal synchrony: a versatile code for the definition of relations? *Neuron.*
865 1999;24: 49–65, 111–25. Available: <http://www.ncbi.nlm.nih.gov/pubmed/10677026>
- 866 60. De Zeeuw CI, Hoebeek FE, Schonewille M. Causes and consequences of oscillations in the
867 cerebellar cortex. *Neuron.* 2008;58: 655–8. doi:10.1016/j.neuron.2008.05.019
- 868 61. Cheron G, Márquez-Ruiz J, Dan B. Oscillations, Timing, Plasticity, and Learning in the
869 Cerebellum. *The Cerebellum.* 2016;15: 122–138. doi:10.1007/s12311-015-0665-9
- 870 62. Dugué GP, Brunel N, Hakim V, Schwartz E, Chat M, Lévesque M, et al. Electrical Coupling
871 Mediates Tunable Low-Frequency Oscillations and Resonance in the Cerebellar Golgi Cell
872 Network. *Neuron.* 2009;61: 126–139. doi:10.1016/j.neuron.2008.11.028
- 873 63. D’Angelo E, Nieuwenhuis T, Maffei A, Armano S, Rossi P, Taglietti V, et al. Theta-frequency bursting
874 and resonance in cerebellar granule cells: experimental evidence and modeling of a slow k^+ -
875 dependent mechanism. *J Neurosci.* 2001;21: 759–70. Available:
876 <http://www.ncbi.nlm.nih.gov/pubmed/11157062>
- 877 64. Hartmann MJ, Bower JM. Oscillatory activity in the cerebellar hemispheres of unrestrained
878 rats. *J Neurophysiol.* 1998;80: 1598–604. Available:
879 <http://www.ncbi.nlm.nih.gov/pubmed/9744967>

- 880 65. Wang Y, Chen H, Hu C, Ke X, Yang L, Xiong Y, et al. Baseline theta activities in medial
881 prefrontal cortex and deep cerebellar nuclei are associated with the extinction of trace
882 conditioned eyeblink responses in guinea pigs. *Behav Brain Res.* 2014;275: 72–83.
883 doi:10.1016/j.bbr.2014.08.059
- 884 66. Rowland NC, Goldberg JA, Jaeger D. Cortico-cerebellar coherence and causal connectivity
885 during slow-wave activity. *Neuroscience.* 2010;166: 698–711.
886 doi:10.1016/j.neuroscience.2009.12.048
- 887 67. Chen H, Wang Y, Yang L, Sui J, Hu Z, Hu B. Theta synchronization between medial prefrontal
888 cortex and cerebellum is associated with adaptive performance of associative learning
889 behavior. *Sci Rep.* 2016;6: 20960. doi:10.1038/srep20960
- 890 68. Courtemanche R, Lamarre Y. Local Field Potential Oscillations in Primate Cerebellar Cortex:
891 Synchronization With Cerebral Cortex During Active and Passive Expectancy. *J Neurophysiol.*
892 2004;93: 2039–2052. doi:10.1152/jn.00080.2004
- 893 69. Frederick A, Bourget-Murray J, Chapman CA, Amir S, Courtemanche R. Diurnal influences on
894 electrophysiological oscillations and coupling in the dorsal striatum and cerebellar cortex of
895 the anesthetized rat. *Front Syst Neurosci.* 2014;8: 145. doi:10.3389/fnsys.2014.00145
- 896 70. Soteropoulos DS, Baker SN. Cortico-Cerebellar Coherence During a Precision Grip Task in the
897 Monkey. *J Neurophysiol.* 2005;95: 1194–1206. doi:10.1152/jn.00935.2005
- 898 71. O'Connor SM, Berg RW, Kleinfeld D. Coherent Electrical Activity Between Vibrissa Sensory
899 Areas of Cerebellum and Neocortex Is Enhanced During Free Whisking. *J Neurophysiol.*
900 2002;87: 2137–2148. doi:10.1152/jn.00229.2001
- 901 72. Colgin LL. Mechanisms and Functions of Theta Rhythms. *Annu Rev Neurosci.* 2013;36: 295–
902 312. doi:10.1146/annurev-neuro-062012-170330
- 903 73. Wikgren J, Nokia MS, Penttonen M. Hippocampo–cerebellar theta band phase synchrony in

- 904 rabbits. *Neuroscience*. 2010;165: 1538–1545. doi:10.1016/j.neuroscience.2009.11.044
- 905 74. Onuki Y, Van Someren EJW, De Zeeuw CI, Van der Werf YD. Hippocampal–Cerebellar
906 Interaction During Spatio-Temporal Prediction. *Cereb Cortex*. 2015;25: 313–321.
907 doi:10.1093/cercor/bht221
- 908 75. Kajikawa Y, Schroeder CE. How Local Is the Local Field Potential? 2011;
909 doi:10.1016/j.neuron.2011.09.029
- 910 76. Basso MA, May PJ. Circuits for Action and Cognition: A View from the Superior Colliculus.
911 *Annu Rev Vis Sci*. 2017;3: 197–226. doi:10.1146/annurev-vision-102016-061234
- 912 77. Proville RD, Spolidoro M, Guyon N, Dugué GP, Selimi F, Isope P, et al. Cerebellum involvement
913 in cortical sensorimotor circuits for the control of voluntary movements. *Nat Neurosci*.
914 2014;17: 1233–1239. doi:10.1038/nn.3773
- 915 78. Cerminara NL, Apps R, Marple-Horvat DE. An internal model of a moving visual target in the
916 lateral cerebellum. *J Physiol*. 2009;587: 429–442. doi:10.1113/jphysiol.2008.163337
- 917 79. Cerminara NL, Apps R. Behavioural significance of cerebellar modules. *Cerebellum*. 2011;10:
918 484–94. doi:10.1007/s12311-010-0209-2
- 919 80. Iseni F, Lafay F, Raux H, Blondel D. Mapping of monoclonal antibody epitopes of the rabies
920 virus P protein. *J Gen Virol*. 1997;78: 119–124. doi:10.1099/0022-1317-78-1-119
- 921 81. Franklin K, Paxinos G. *The mouse brain in stereotaxic coordinates*. 3rd ed. Elsevier; 2007.
- 922 82. de Lavilléon G, Lacroix MM, Rondi-Reig L, Benchenane K. Explicit memory creation during
923 sleep demonstrates a causal role of place cells in navigation. *Nat Neurosci*. *Nature Research*;
924 2015;18: 493–495. doi:10.1038/nn.3970
- 925 83. Carlezon WA, Chartoff EH. Intracranial self-stimulation (ICSS) in rodents to study the
926 neurobiology of motivation. *Nat Protoc*. 2007;2: 2987–2995. doi:10.1038/nprot.2007.441

- 927 84. Lasztóczy B, Klausberger T. Hippocampal Place Cells Couple to Three Different Gamma
928 Oscillations during Place Field Traversal. *Neuron*. 2016;91: 34–40.
929 doi:10.1016/j.neuron.2016.05.036
- 930 85. Bokil H, Andrews P, Kulkarni JE, Mehta S, Mitra PP. Chronux: A platform for analyzing neural
931 signals. *J Neurosci Methods*. 2010;192: 146–151. doi:10.1016/j.jneumeth.2010.06.020
- 932 86. Islam MK, Rastegarnia A, Nguyen AT, Yang Z. Artifact characterization and removal for in vivo
933 neural recording. *J Neurosci Methods*. 2014;226: 110–123.
934 doi:10.1016/j.jneumeth.2014.01.027
- 935
- 936

937 **Figure Legends**

938

939 **Figure 1. Topographically restricted regions of cerebellar cortex are connected to the**
940 **hippocampus.**

941 **A**, Left, mean number of labeled cells in the deep cerebellar nuclei (DCN), vestibular nuclei
942 (VN) and cerebellar cortex at different survival times following rabies injection in left
943 hippocampal dentate gyrus. Box shows a magnification of the labeling at 48 and 58 h (n = 5
944 mice for all data points except 48 h, n = 3). Middle, schematic representation of rabies
945 injection site and survival times required to reach the cerebellar and vestibular nuclei (58 h,
946 dashed blue line, polysynaptic pathway), and cerebellar cortex (66 h, orange line). Upper
947 right, schematic view of the posterior cerebellar cortex indicating regions of highest labeling
948 following rabies virus injection (red, vermis lobule VI; green, Crus I; grey, paraflocculus). **B-E**,
949 Representative photomicrographs showing labeling in the contralateral cerebellar and
950 vestibular nuclei 58 h post infection. Left panels show low magnification view, right panels
951 show magnified view of area indicated by dashed box. Solid arrow heads indicate the
952 presence of the very few labeled cells in the IntP. **F**, Pooled, normalized counts of rabies
953 labeled cells in the ipsi- and contralateral cerebellar and vestibular nuclei 58 h post infection
954 (n = 5 mice). No significant differences were found between ipsi- and contralateral nuclei
955 (nuclei x hemisphere two-way ANOVA, hemisphere effect $F_{(1, 4)} = 1.31 \times 10^{-5}$, $p = 0.99$,
956 interaction effect $F_{(3, 12)} = 2.79$, $p = 0.09$, nuclei effect $F_{(3, 12)} = 9.38$, $p = 0.002$). **G**,
957 Normalised cell counts in the fastigial nucleus (left) and dentate nucleus (right), according to
958 their rostro-caudal position relative to bregma. Open circles, contralateral count; filled
959 circles, ipsilateral count (n= 5 mice). **H-K**, Representative photomicrographs of the resultant
960 labeling in lobule VI, Crus I, paraflocculus and lobule II at 66 h post infection. **L**, Normalised
961 count of rabies labeled cells in anterior (black bar; lobule II to lobule IV/V); central (dark
962 grey bar; lobule VI to Crus II); posterior (clear bar; lobule VIII and lobule IX) and
963 flocculonodular (Floc. Nod., light grey bar; lobule X, flocculus and paraflocculus) cerebellum
964 66 h post infection (n= 5 mice; one-way ANOVA with FDR correction, $F_{(3, 16)} = 19.11$, $p <$
965 0.0001). **M**, Normalised cell count of rabies labelled cells in all assessed lobules 66 h post
966 infection. Colour coding of bars indicate assignment of lobules to either anterior, central,
967 posterior or vestibular cerebellum as indicated in **L**. Abbreviations: Dent., Dentate nucleus;
968 Fast., fastigial nucleus; Fast. DL, dorsolateral fastigial nucleus; Floc. Nod., flocculonodular

969 lobe; Interp., nucleus interpositus; IntA, nucleus interpositus anterior; IntDL, dorsolateral
970 nucleus interpositus; IntP, nucleus interpositus posterior; i-Sim, ipsilateral simplex lobule; c-
971 Sim, contralateral simplex lobule; i-Crus I, ipsilateral Crus I; c-Crus I, contralateral Crus I; i-
972 Crus II, ipsilateral Crus II; c-Crus II, contralateral Crus II; i-Par, ipsilateral paramedian lobule;
973 c-Par, contralateral paramedian lobule; i-CP, ipsilateral copula; c-CP, contralateral copula; i-
974 Floc, ipsilateral flocculus; c-Floc, contralateral flocculus; i-PF, ipsilateral paraflocculus; c-PF,
975 contralateral paraflocculus; Vestib., vestibular nuclei. ** $q < 0.01$, *** $q < 0.001$.

976

977

978 **Figure 2. Different cerebellar modules project to the hippocampus.**

979 **A**, 3-D reconstruction showing the location of RABV+ Purkinje cells in the most labeled
980 cerebellar lobules at 66 h post-infection. Red, blue and green dots represent RABV+ Purkinje
981 cells in lobule VI, Crus I and paraflocculus, respectively. **B**, Photomicrographs from case S18
982 showing double staining against zebrin II (green, left column), RABV (red, central column)
983 and merge (right column) in lobule VI (i), Crus I (ii and iii) and paraflocculus (iv). RABV+
984 Purkinje cells were also zebrin positive and were organized in clusters of strongly labeled
985 RABV+ cells (filled arrow-heads) surrounded by weakly labeled RABV+ Purkinje cells (unfilled
986 arrow-heads). **C**, Assignment of the RABV+ clusters to specific cerebellar modules for case
987 S18 in the anterior (AZ; left), central (CZ; central column) and posterior (PZ; right column)
988 zones. First row shows stacked sections with zebrin positive Purkinje cells (white dots) and
989 RABV+ Purkinje cells, which were also zebrin positive (purple dots, strong and weakly
990 labeled cells included); central row shows reconstructed principal zebrin bands (delineated
991 by yellow dashed lines and named from 1+ to 7+; nomenclature from [42] and cerebellar
992 modules (capital letters; defined as in [42])); and bottom row shows the location of the
993 RABV+/zebrin Purkinje cells (purple dots) in relation to reconstructed zebrin bands and
994 modules. Abbreviations, I, lobule I; III, lobule III; IV/V, lobule IV/V; VIa and VI b-c, lobule VIa
995 and VI b-c, respectively; IX, lobule IX; X, lobule X; Sim, lobule simplex; Cr I, Crus I; Cr II, Crus
996 II; Par, paramedian lobule; CP, copula, PFL, paraflocculus, FL, flocculus.; dPFC and vPFC,
997 dorsal and ventral paraflocculus, respectively.

998

999

1000 **Figure 3. Assessment of cerebello-hippocampal interactions during active movement in**
1001 **the home-cage.**

1002 **A**, Schematic representation of recording and stimulation electrode implant positions. **B**,
1003 Representative simultaneous LFP and EMG recording made during active movement in the
1004 home-cage condition. Colored lines: raw LFP (filtered from 0.1 to 600 Hz). Overlaid grey lines:
1005 LFP filtered from 6-12 Hz. Note prominent 6-12 Hz oscillations in left hippocampal recording
1006 and deflections on neck EMG trace, reflecting active movement (EMG rectified and
1007 smoothed to 2.5 ms). **C**, Pooled z-score of the power spectra of hippocampal LFP recorded
1008 from the left (n = 16 mice) and right (n= 18 mice) hemispheres during home-cage exploration
1009 and from cerebellar Crus I (n = 12), lobule II/III (n = 10) and lobule VI (n = 18). **D**, Pooled
1010 coherence between cerebellar cortical regions (colour coded) and hippocampus (left, Crus I,
1011 n = 11; lobule II/III, n = 8; lobule VI, n = 15; right, Crus I, n = 11; lobule II/III, n = 9; lobule VI, n
1012 = 16) during home-cage exploration. **E**, Mean cerebello-hippocampal coherence in the 6-12
1013 Hz range (Crus I, n = 21 values/12mice; lobule II/III, n = 17 values/10 mice; lobule VI, n = 31
1014 values/18 mice). Lobule VI-hippocampus coherence level was significantly higher than that
1015 observed with lobule II/III (*, $q < 0.05$; Kruskal-Wallis with FDR correction). **F**, Mean 6-12 Hz
1016 coherence between lobule VI and hippocampus plotted against estimated medio-lateral
1017 recording electrode position in lobule VI (red dots; n = 16 mice, coherence with right and
1018 left hippocampus pooled; linear regression, $R^2 = 0.348$, $p < 0.001$). In grey, number of RABV+
1019 cells counted across lobule VI, 66 h after injection in the left hippocampus as a function of
1020 medio-lateral position (0.2 mm bins; n = 5 mice). Shading indicates S.E.M. Abbreviations,
1021 LFP, local field potential; HPC, dorsal hippocampus; lob II/III, lobule II/III; lob VI, lobule VI;
1022 EMG, electromyogram.

1023

1024

1025 **Figure 4. Cerebello-hippocampal interactions during goal-directed behavior**

1026 **A**, Mice learned to traverse a 1 m linear track to receive a medial forebrain bundle
1027 stimulation upon reaching invisible goal zones (lightening symbols indicate MFB stimulation;
1028 n = 8 mice). Representative trajectories from early (trial 1) and late training (trial 20) show
1029 the transition from exploratory to goal-directed behavior. **B**, Mice improved their
1030 performance in the task across trials as shown by increases in the mean number of rewards
1031 obtained (purple line; plotted against left Y axis; one-way repeated measures ANOVA, time

1032 effect $p < 0.0001$) and the mean speed (orange line; plotted against the right Y axis; one-way
1033 repeated measures ANOVA, time effect $p = 0.0098$).**C**, Mean z-score 6-12 Hz power of the
1034 recorded LFP signals (colour coded; Crus I, $n = 5$; lobule II/III, $n = 6$; lobule VI, $n = 7$; HPC left
1035 , $n = 6$; HPC right, $n = 7$; left and right HPC values are pooled as no difference was observed
1036 across hemispheres, hemisphere x trial two-way ANOVA with FDR correction, hemisphere
1037 effect $p = 0.5974$, interaction effect $p = 0.3132$, trial effect $p < 0.0001$) across trials. Solid
1038 blue line indicate trials where hippocampus values were significantly higher than those in
1039 trial 1 ($q < 0.05$).**D**, Mean coherence in the 6-12 Hz range between cerebellar regions (colour
1040 coded) and hippocampus (pooled bilaterally) during learning of the linear track task (Crus I,
1041 $n = 8$ values/5 mice; lobule II/III, $n = 9$ values/6 mice; lobule VI, $n = 12$ values/7 mice).
1042 Significant changes in coherence were observed over trials (combination x trial two-way
1043 ANOVA with FDR correction, trial effect $p < 0.001$, combination effect $p = 0.0285$,
1044 interaction effect $p < 0.0001$). Solid green rectangles indicates trials where Crus I-
1045 hippocampus coherence was higher than those in trial 1 ($q < 0.05$). This increase in Crus I-
1046 hippocampus coherence was also reflected in significant changes relative to other lobules:
1047 grey bordered rectangle corresponds to trials significantly higher than lobule II/III-
1048 hippocampus coherence ($q < 0.05$) while red bordered rectangles indicates those
1049 significantly higher than lobule VI-hippocampus coherence ($q < 0.05$). **E-F**, Pooled power
1050 spectra from hippocampal and cerebellar LFPs (z-score normalized, colour coded) from
1051 representative trials of early (**E**; trial 1) and late (**F**; trial 20) stages of training. **G-H**, Pooled
1052 coherence between cerebellar cortical regions and bilateral hippocampus from
1053 representative trials of early (**G**; trial 1) and late (**H**; trial 20) stages of training. Shading
1054 indicates S.E.M. Abbreviations, HPC, dorsal hippocampus; lob II/III, lobule II/III; lob VI, lobule
1055 VI.

1056

1057

1058 **Figure 5. Cerebello-hippocampal interaction dynamics**

1059 Mean 6-12 Hz coherence for each cerebello-hippocampal recording combination (Crus I, $n =$
1060 8 values/5 mice; lob II/III, $n = 9$ values/6 mice; lob VI, $n = 12$ values/7 mice) obtained during
1061 homecage recordings before training in the linear track (HC pre LT), during a representative
1062 trial of early training in the linear track (trial 1; early LT), during a representative trial of late
1063 training in the linear track (trial 20; late LT) and during homecage recording following

1064 completion of linear track training (HC post LT). A significant increase in Crus I–hippocampus
1065 coherence was observed during late LT compared to both HC pre LT and early LT, which
1066 then returned to pre-training levels during HC post LT (paired Friedman test with FDR
1067 correction, $p = 0.0037$; * $q < 0.05$, ** $q < 0.01$). Lobule VI - hippocampus and lobule II/III -
1068 hippocampus coherence levels did not change significantly across conditions (paired
1069 Friedman test, FDR corrected p-value = 0.1718 and 0.5319, respectively). Abbreviations, lob
1070 II/III, lobule II/III; lob VI, lobule VI.

1071

1072 **Figure 6. Cerebello-hippocampal coherence patterns during goal-directed behavior in**
1073 **virtual reality.**

1074 **A**, Schematic of the virtual reality system and recording setup. Head-fixed mice were trained
1075 to move an air-cushioned Styrofoam ball in order to navigate through a virtual environment
1076 displayed on six TFT monitors surrounding the animal. **B**, Example recording of the virtual
1077 position as a mouse traversed a virtual linear track to receive rewards (MFB stimulation
1078 indicated by a lightning symbol, $n = 7$). **C**, Behavioural performance remained stable across
1079 trials as illustrated by the mean number of rewards (purple line; plotted against left Y axis;
1080 one-way repeated measures ANOVA, $p = 0.4070$) and the mean speed (orange line; plotted
1081 against the right Y axis; one-way repeated measures ANOVA, $p = 0.4583$). **D**, Pooled, z-
1082 scored normalized power spectra of hippocampal LFP recorded from the left ($n = 16$ mice)
1083 and right ($n = 18$ mice) hemispheres during homecage exploration and from cerebellar Crus I
1084 ($n = 12$), lobule II/III ($n = 10$) and lobule VI ($n = 18$). **E**, Averaged coherence between
1085 cerebellar cortical regions (colour coded) and bilateral hippocampus, pooled across all trials
1086 (Crus I-HPC, $n = 5$ values/3 mice; lobule II/III-HPC, $n = 8$ values/5 mice; lobule VI-HPC, $n = 9$
1087 values/5 mice). **F**, Mean cerebello-hippocampal coherence in the 6-12 Hz frequency range.
1088 Both lobule VI and Crus I showed significantly higher coherence with hippocampus than
1089 lobule II/III (Kruskal Wallace with FDR correction, $p = 0.0137$; ** $q < 0.01$). Shading indicates
1090 S.E.M.

1091

1092 **Figure 7. Comparison of cerebello-hippocampal interactions during epochs of similar**
1093 **behavioural performances in real-world and virtual-reality conditions.**

1094 **A**, For each mouse ($n = 6$) we selected one trial from the real world linear track (LT) and one
1095 from the virtual reality (VR) condition in which behavioural performance was similar, as
1096 defined by non-significant changes in the number of rewards obtained (purple circles;
1097 plotted against left Y axis; paired t test, $p = 0.5279$) or the mean speed (orange circles;
1098 plotted against right Y axis; paired t test, $p = 0.6119$). **B**, Overall coherence between
1099 cerebellar cortical regions (colour coded) and bilateral hippocampus (Crus I, $n = 5$ values/3
1100 mice; lobule II, $n = 8$ values/5 mice; lobule VI, $n = 9$ values/5 mice) in the selected trials from
1101 the linear track. **C**, Same as in **B** but for the selected trials from the virtual reality. **D**, For
1102 each recording combination, we compared 6-12Hz coherence values obtained from the
1103 selected linear track and virtual reality epochs. Crus I levels were significantly reduced in the
1104 virtual reality trials compared with the linear track (paired t test, *, $p = 0.0480$) while lobule
1105 VI or lobule II/III levels were similar in both conditions (Paired t tests, $p = 0.1465$ and 0.4165 ,
1106 respectively).

1107

1108 **Figure S1. Location of rabies virus injection for the 4 experimental groups.**

1109 RABV was co-injected with fluorescent CTB to visualize the injection spread. The location of
1110 the injection is indicated by the red area on a standard coronal outline of the left
1111 hippocampus adapted from [81]. Rostro-caudal position relative to bregma is indicated on
1112 the left (mm). Experimental ID for each case is shown above the sections. **A**, Injection sites
1113 of the 5 mice from the 30h survival time group **B**, Injection sites of the 3 mice from the 48h
1114 survival time group. **C**, Injection sites of the 5 mice from the 58h survival time group. **D**,
1115 Injection sites of the 5 mice from the 66h survival time group.

1116

1117 **Figure S2. Rabies virus main labelled structures 30h after hippocampal rabies injection.**

1118 **A**, Cumulative sum of labelled cells per structure after 30h post hippocampal rabies
1119 injection (colour coded for each case, $n = 5$ mice). **B-C**, Localisation and representative
1120 photomicrographs of RABV most labelled regions at 30h, lateral entorhinal cortex (**B**) and
1121 nucleus of the diagonal band (**C**). The position is indicated by a blue insert on a standard
1122 coronal brain section adapted from [81], and rostro-caudal position according to Bregma is
1123 indicated in the top-right corner. Abbreviations, ADN, antero-dorsal nucleus of the
1124 thalamus; LDN, latero-dorsal nucleus of the thalamus; Lat entorhinal cortex, lateral
1125 entorhinal cortex; NDB, nucleus of the diagonal band; TRN, thalamic reticular nucleus.

1126

1127 **Figure S3. The topographical distribution of DCN labelling at 66h.**

1128 **A-D**, representative photomicrographs showing labeling in the ipsilateral cerebellar and
1129 vestibular nuclei 66h after hippocampal rabies injection. Left panels show low magnification
1130 view, right panels show high magnification view of area indicated by dashed box. **E**, Pooled,
1131 normalized counts of rabies labeled cells in the ipsi- and contralateral cerebellar and
1132 vestibular nuclei (n = 5 mice). No significant differences were found between ipsi- and
1133 contralateral nuclei (nuclei x hemisphere two-way ANOVA, hemisphere effect $F_{(1, 4)} = 1.14$, p
1134 = 0.35, interaction effect $F_{(3, 12)} = 0.21$, $p = 0.89$, nuclei effect $F_{(3, 12)} = 7.88$, $p = 0.004$). **F**,
1135 Normalized cell counts in the fastigial nucleus (left) and dentate nucleus (right) according to
1136 their rostro-caudal position relative to Bregma. Open circles, contralateral count; filled
1137 circles, ipsilateral count (n = 5 mice). Abbreviations: Dent., Dentate nucleus; Fast., fastigial
1138 nucleus; Fast. DL, dorsolateral fastigial nucleus; Interp., nucleus interpositus; IntA, nucleus
1139 interpositus anterior; IntDL, dorsolateral nucleus interpositus; IntP, nucleus interpositus
1140 posterior; Vestib., vestibular nuclei.

1141

1142 **Figure S4. Reconstructed location of the implanted electrodes.**

1143 The position of the implanted electrodes are represented by black dots on a standard
1144 sagittal outline of the cerebellum (**A**) or coronal outline of the hippocampus (**B**) [adapted
1145 from 81]. The medio-lateral (in **A**) or rostro-caudal (in **B**) positions relative to midline or
1146 bregma, respectively, are indicated next to the outlines. Abbreviations, II, lobule II; III, lobule
1147 III; IV/V, lobule IV/V; VI, lobule VI; VII, lobule VII; VIII, lobule VIII; IX, lobule IX; X, lobule X;
1148 Sim, lobule simplex; PM, paramedian lobule.

1149

1150 **Figure S5. Cerebello-hippocampal coherence patterns are similar across hemispheres**
1151 **during active movement in homecage.**

1152 **A**, Schematic indicating approximate distances between recording sites in the cerebellum
1153 and left/right dorsal hippocampus (HPC). **B**, Overall power spectra from right (n = 18) and
1154 left (n = 16) HPC and cerebellar recordings made from Crus I (n = 12), lobule II/III (n = 10)
1155 and lobule VI (n = 18) during active movement in the homecage environment. **C**, Overall
1156 coherence between cerebellar cortical regions (Crus I, n = 11; lobule II, n = 8; lobule VI, n =
1157 15; colour coded) and left HPC during active homecage movement. **D**, Overall coherence

1158 between cerebellar cortical regions (Crus I, n = 10; lobule II, n = 9; lobule VI, n = 16; colour
1159 coded) and right HPC. **E**, Mean 6-12 Hz coherence between cerebellar recordings and left or
1160 right HPC. No differences were observed between hemispheres (hemisphere x combination
1161 one-way ANOVA with FDR correction, hemisphere effect $p = 0.6355$). **F**, The number of
1162 12min analysis blocks was not correlated to the mean 6-12 Hz level of coherence obtained.
1163 Coherence values shown for all cerebello-hippocampal recording combinations (n= 57
1164 values/23 mice; solid line indicates linear regression; dashed lines indicate 95% confidence
1165 intervals). Shading indicates S.E.M.

1166

1167 **Figure S6. Transient 6-12 Hz oscillations are present in the cerebellar cortex.**

1168 **A**, Upper trace, 200s epoch of LFP (0.1 to 600Hz) recorded from lobule VI during active
1169 movement in the homecage environment. Lower panel, spectrogram of the LFP. Periods of
1170 intense spectral power in the 6-12Hz band demarked by red boxes. **B**, 20s period of intense
1171 oscillation (from area marked by dashed white lines in **A**) is shown on a larger timescale. In
1172 red, same epoch filtered in the 6-12 Hz frequency band. **C**, Power spectra calculated from
1173 the whole period (black line), from epochs of high intensity in the 6-12Hz frequency band
1174 (epochs demarked by red boxes in **A**; red line) and from epochs without high intensity in the
1175 6-12Hz frequency band (blue line). Arrow indicates peak in spectra within the 6-12Hz range,
1176 apparent in the selected high intensity periods.

1177

1178 **Figure S7. Cerebello-hippocampal coherence patterns are conserved across hemispheres**

1179 **during running on the linear track.** **A**, Mean z-score 6-12 Hz power of the recorded LFPs
1180 from left (n = 6) and right (n = 5) hippocampus (HPC) and from the cerebellum (colour
1181 coded; Crus I, n = 5; lobule II/III, n = 6; lobule VI, n = 7) across trials. No laterality effect was
1182 found in the HPC (hemisphere x trial two-way ANOVA with FDR correction, hemisphere
1183 effect $p = 0.5974$, interaction effect $p = 0.3132$, trial effect $p < 0.0001$). Solid blue line
1184 indicate trials where HPC values were significantly higher than those in trial 1 ($q < 0.05$). **B**,
1185 Over trials, there was a significant increase in the peak frequency of the power spectra in
1186 both left and right HPC recordings; however, no differences were found between
1187 hemispheres (hemisphere x trial two-way ANOVA with FDR correction, trial effect $p <$
1188 0.0001 , hemisphere effect $p = 0.4124$, interaction effect $p > 0.9999$; solid blue line shows
1189 trials significantly different from trial 1, $q < 0.05$). **C**, No differences were observed in the

1190 mean 6-12 Hz coherence between left or right HPC and Crus I at early (trial 1) or late (trial
1191 20) stages of training (Crus I-HPC left, n = 4; Crus I-HPC right, n = 4; hemisphere x trial two-
1192 way ANOVA, hemisphere effect p = 0.9026, interaction effect p = 0.7272, trial effect p =
1193 0.0183). **D**, Peak frequency of cerebello-hippocampal coherence was not affected by the
1194 hippocampal hemisphere and did not change across trials for any combination (colour
1195 coded; Crus I-HPC left, n = 4, Crus I-HPC right, n = 4, hemisphere x trial two-way ANOVA,
1196 hemisphere effect p = 0.3601, interaction effect p = 0.9652, trial effect p = 0.2954; lobule
1197 II/III-HPC left, n = 4, lobule II/III-HPC right, n = 5, hemisphere x trial two-way ANOVA,
1198 hemisphere effect p = 0.2485, interaction effect p = 0.5048, trial effect p = 0.1767; lobule VI-
1199 HPC left, n = 6, lobule VI-HPC right, n = 6, hemisphere x trial two-way ANOVA, hemisphere
1200 effect p = 0.7025, interaction effect p = 0.9446, trial effect p = 0.2543). Shading indicates
1201 S.E.M.

1202

1203

1204 **Figure S8. Speed and power spectrum dynamics across homecage and real world linear**
1205 **track conditions.**

1206 **A**, Significant changes in speed were found across all conditions (HC pre LT, early and late LT
1207 and HC post LT; one-way repeated measures ANOVA with FDR correction, n = 8 mice). **B**, No
1208 significant differences were observed in hippocampal 6-12Hz z-score power (pooled values
1209 from both hemispheres) across conditions (repeated measures Friedman test, p = 0.1764, n
1210 = 13). **C**, No significant differences were observed across conditions in 6-12 Hz z-score
1211 power of Crus I (repeated measures Friedman test, p = 0.0755, n = 5), lobule VI (repeated
1212 measures Friedman test, p = 0.4188, n = 7) or lobule II/III (repeated measures Friedman test,
1213 p = 0.3751, n = 6). * q < 0.05, ** q < 0.01, *** q < 0.001. Abbreviations as for Fig. 5.

1214

1215

1216 **Figure S9. Cerebello-hippocampal coherence patterns are similar across hemispheres**
1217 **during goal-directed behavior in virtual reality.**

1218 **A**, Peak frequency of the power spectra from left (n = 4) and right (n = 6) hippocampus
1219 (HPC) across trials. There was no difference between hemispheres but there was a
1220 significant effect of the trial (hemisphere x trial two-way ANOVA with FDR correction, trial
1221 effect p = 0.004, hemisphere effect p = 0.8795, interaction effect p = 0.9998). **B**, Mean z-

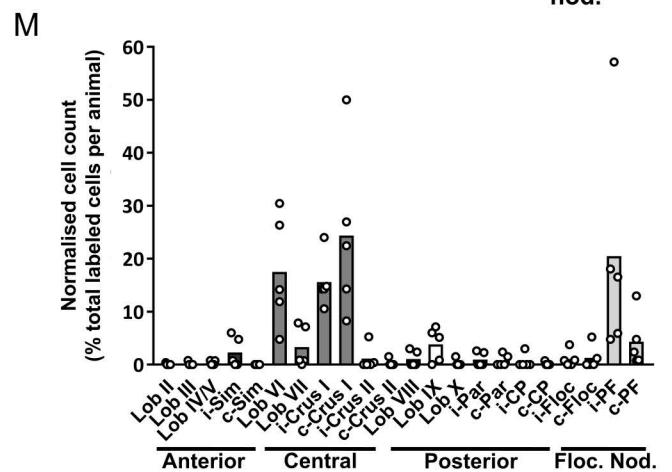
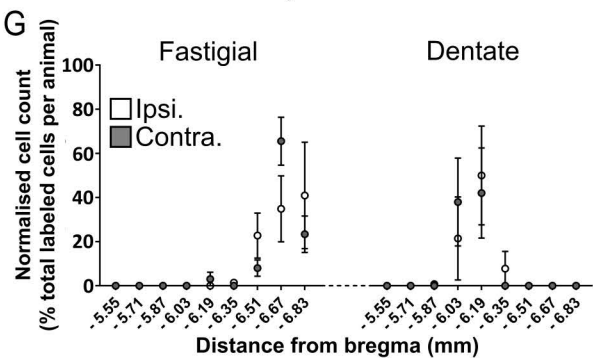
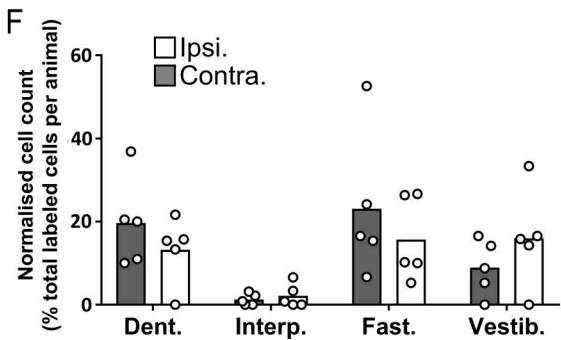
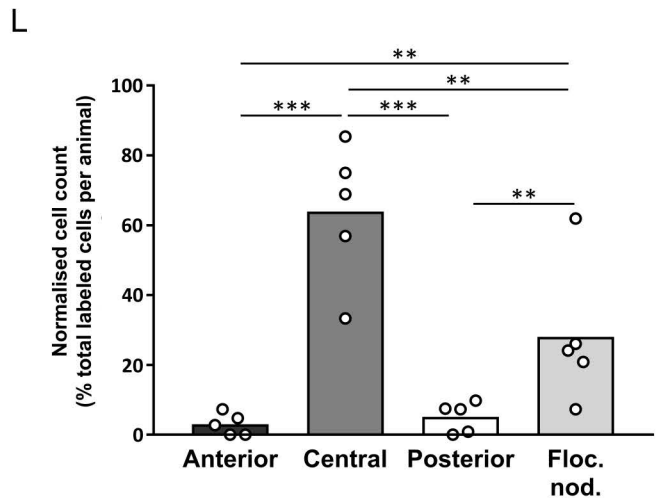
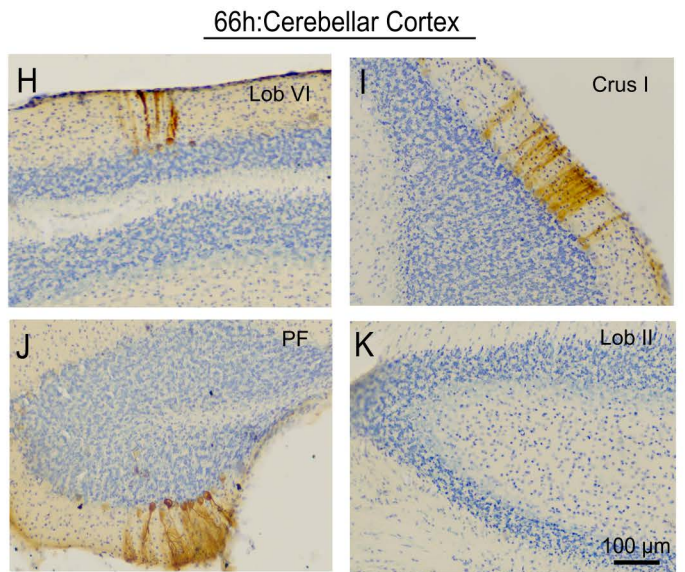
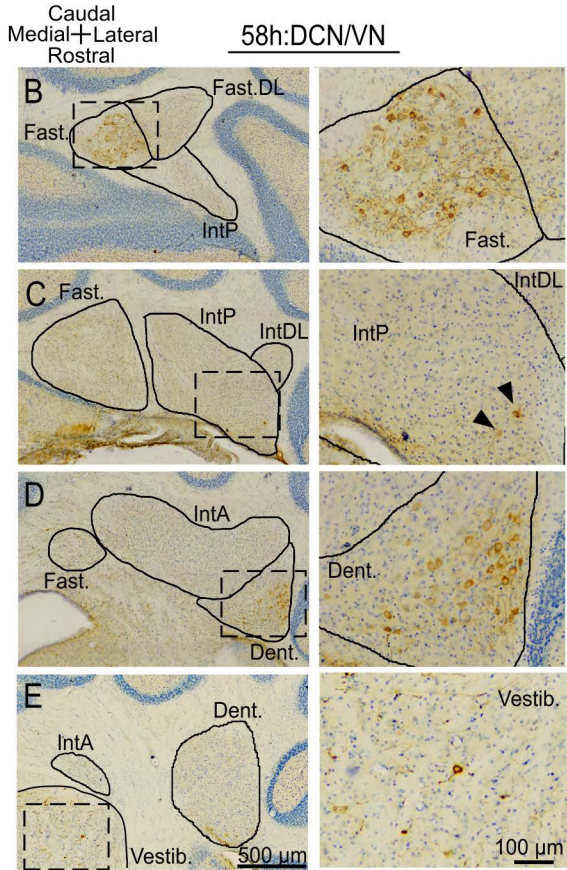
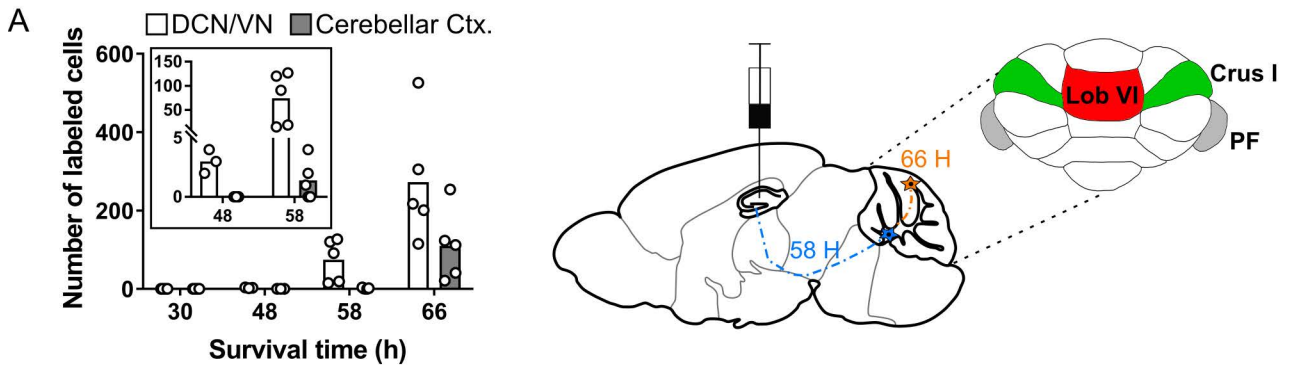
1222 score 6-12 Hz LFP power (colour coded; Crus I, n = 3; lobule II/III, n = 5; lobule VI, n = 5)
1223 across trials. No laterality effect or trial effect was found in the HPC (hemisphere x trial two-
1224 way ANOVA with FDR correction, hemisphere effect $p = 0.7357$, interaction effect $p =$
1225 0.9865 , trial effect $p = 0.4180$). Similarly, no differences were observed between cerebellar
1226 regions and no changes across trials (cerebellar region x trial two-way ANOVA with FDR
1227 correction, cerebellar region effect $p = 0.8290$, interaction effect $p = 0.9993$, trial effect $p =$
1228 0.1781). **C**, Pooled, mean 6-12 Hz cerebello-hippocampal coherence (colour coded; Crus I-
1229 HPC = 5 values/3mice, lobule II/III = 8 values/5 mice, lobule VI-HPC = 9 values/5mice) across
1230 trials in the virtual reality condition. No differences across trials were observed at any
1231 cerebello-hippocampal combination (cerebellar region x trial two-way ANOVA with FDR
1232 correction, trial effect $p = 0.0724$, interaction effect $p = 0.1265$). **D**, Overall z-score power
1233 spectrum from cerebellar cortical regions (colour coded) and bilateral HPC averaged across
1234 all trials. **E**, Overall coherence between cerebellar cortical regions (Crus I, n = 2; lobule II/III,
1235 n = 3; lobule VI, n = 4; colour coded) and left HPC averaged across all VR trials. **F**, Overall
1236 coherence between cerebellar cortical regions (Crus I, n = 3; Lobule II/III, n = 5; Lobule VI, n
1237 = 5; colour coded) and right HPC. **G**, Mean 6-12 Hz coherence between cerebellar recordings
1238 and left or right HPC. No differences were observed between hemispheres (hemisphere x
1239 combination one-way ANOVA with FDR correction, hemisphere effect $p = 0.6355$). Shading
1240 indicates S.E.M.

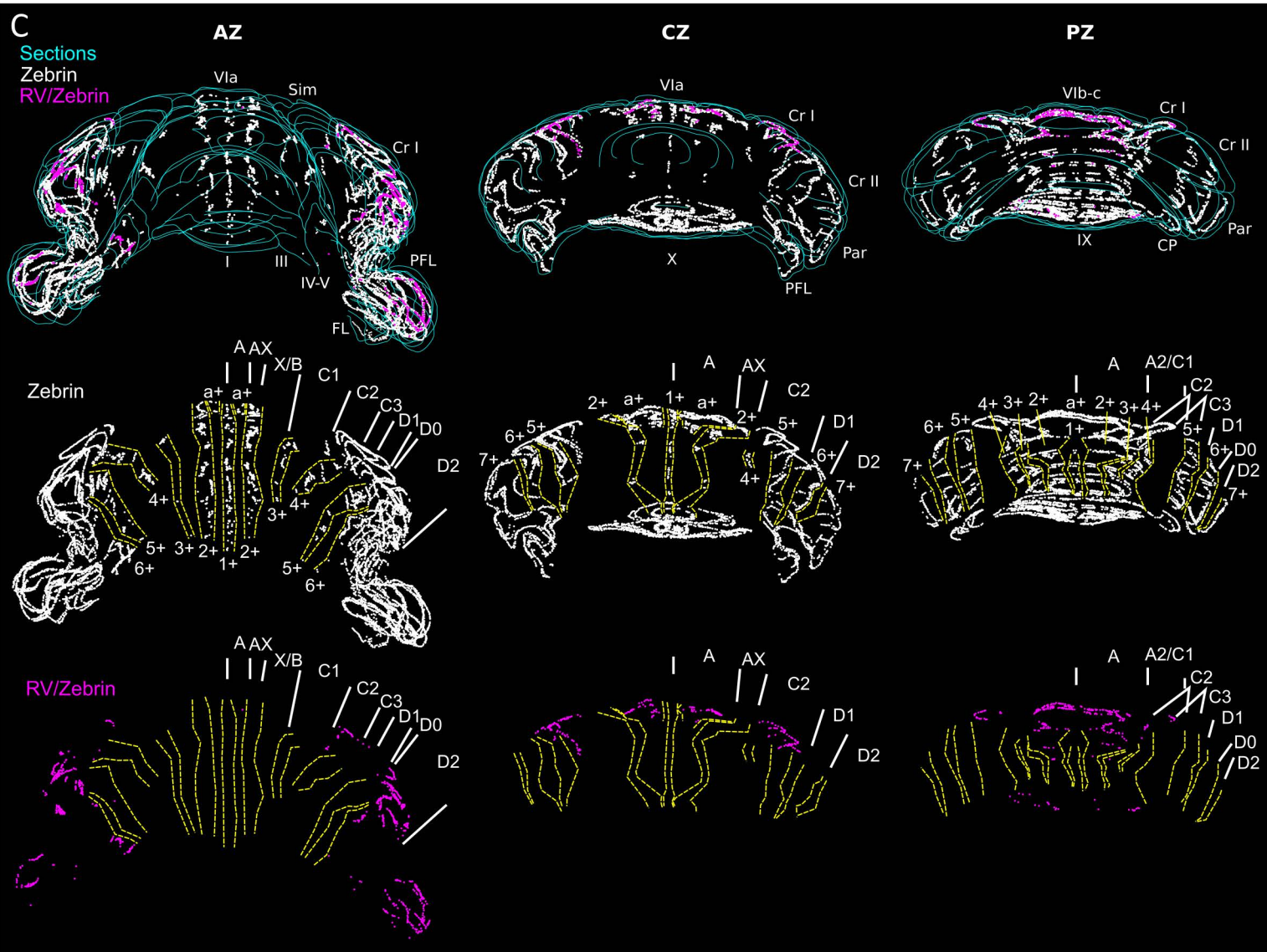
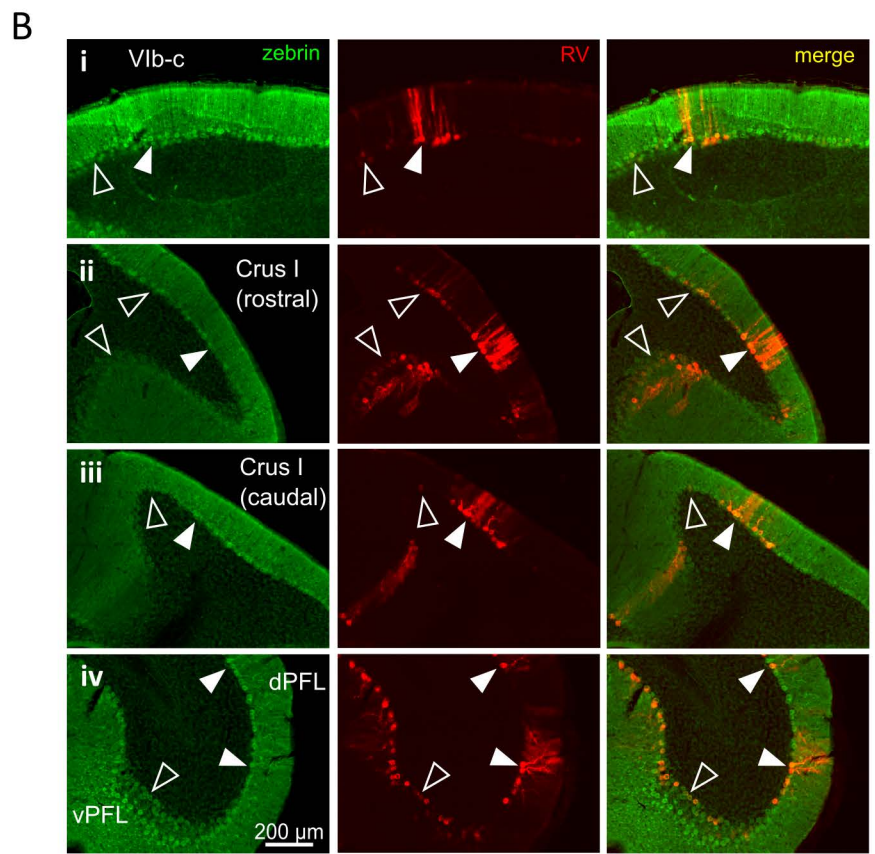
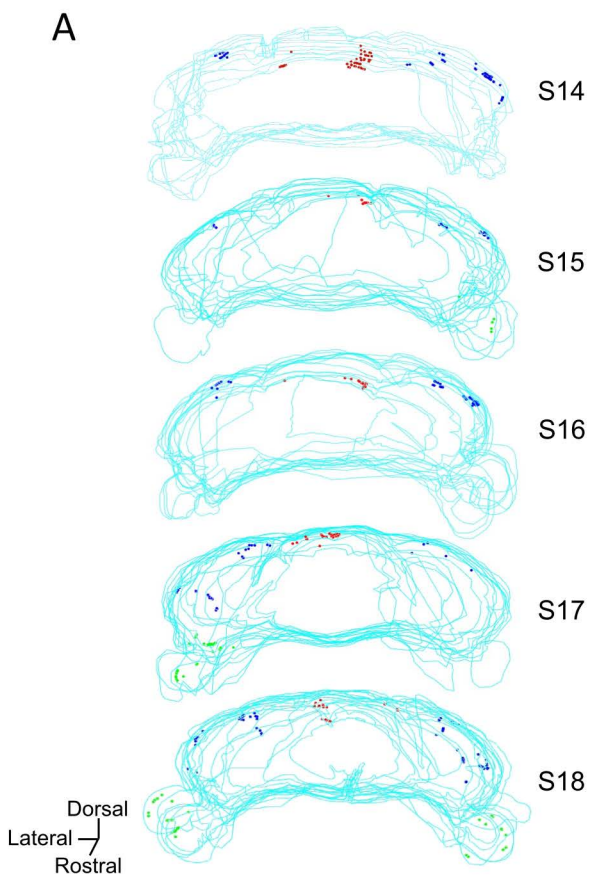
1241

1242 **Table 1**

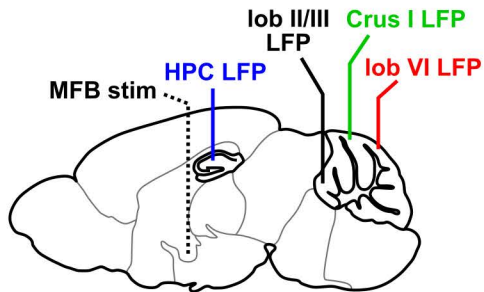
1243 Overview of RABV labeling intensity in different brain regions for all animals in the four
1244 experimental groups (30h, 48h, 58h and 66h post RABV injection). (-) denotes no labeling,
1245 (+/-) few cells, (+) minor labeling, (++) fair labeling, (+++) strong labelling. Question mark
1246 indicates that the area was not available for analysis. When the labeling was different
1247 between ipsilateral (i.) and contralateral (c.) hemispheres, the regions are split in two
1248 columns.

1249

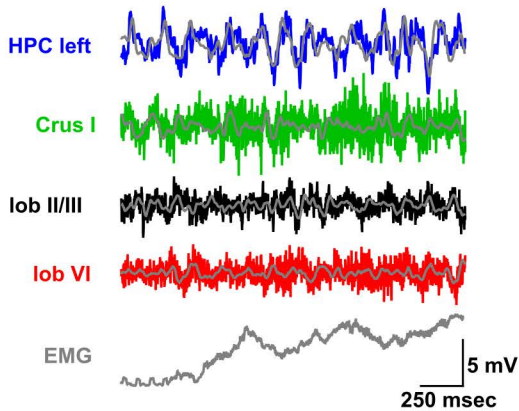




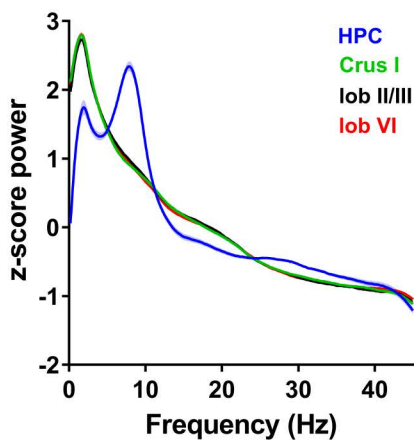
A



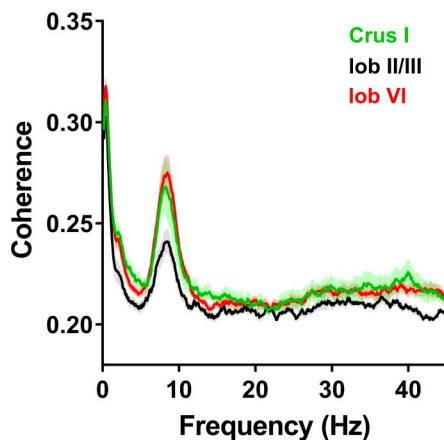
B



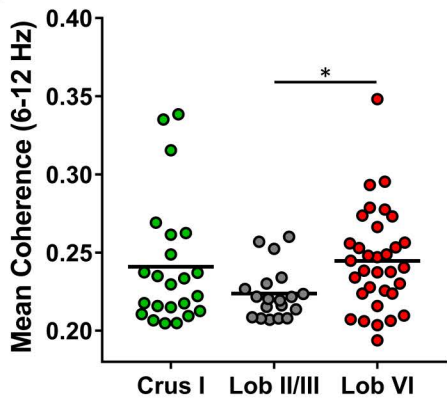
C



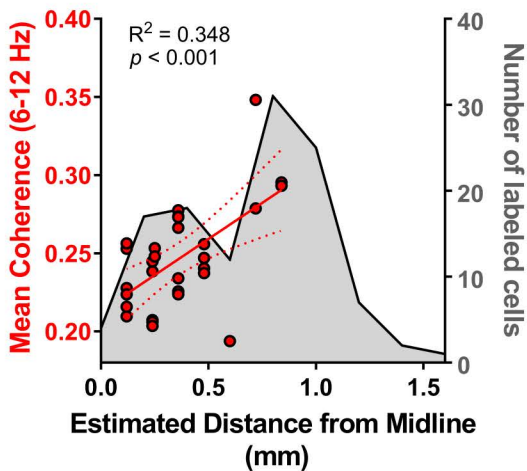
D

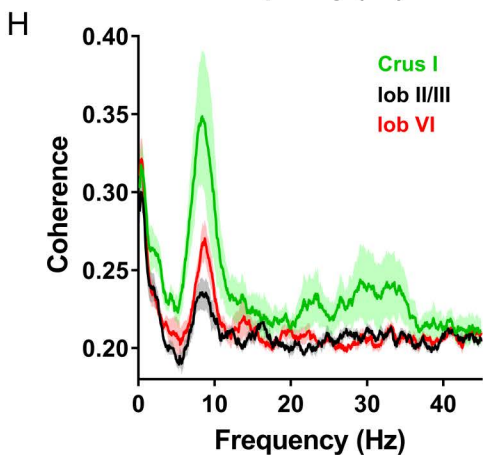
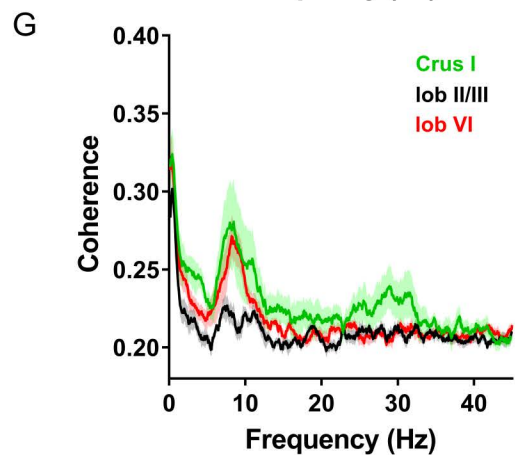
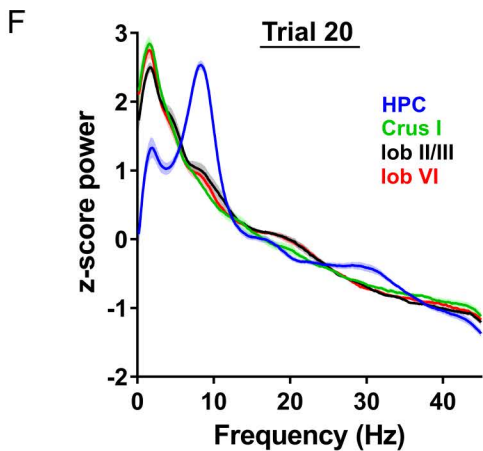
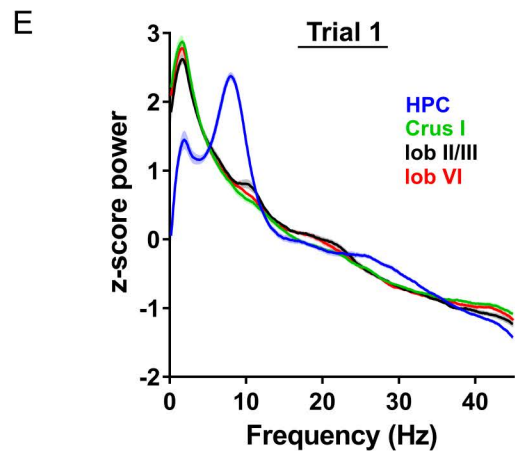
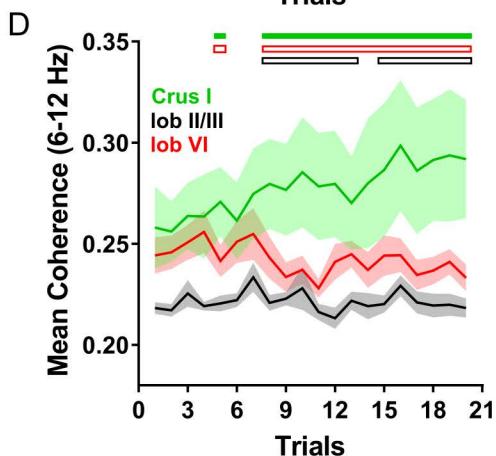
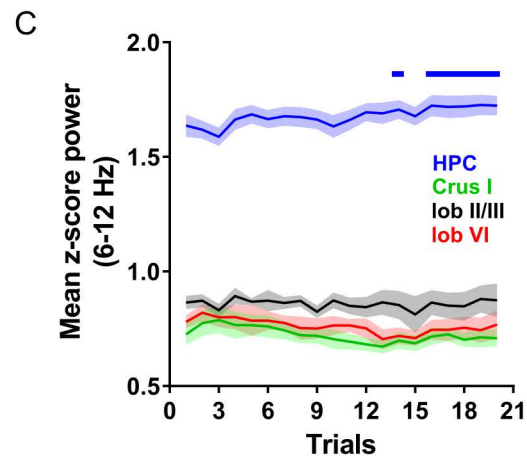
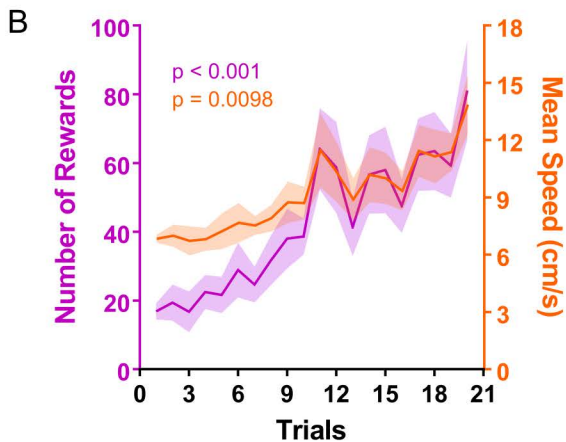
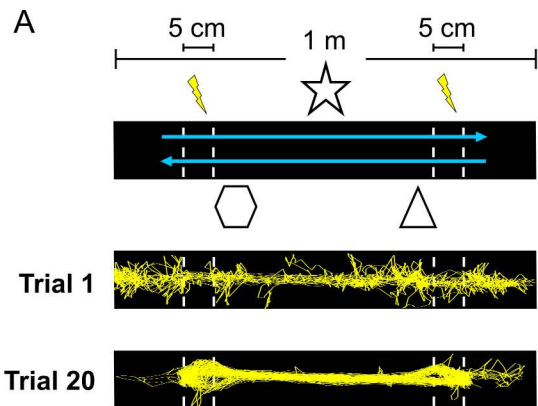


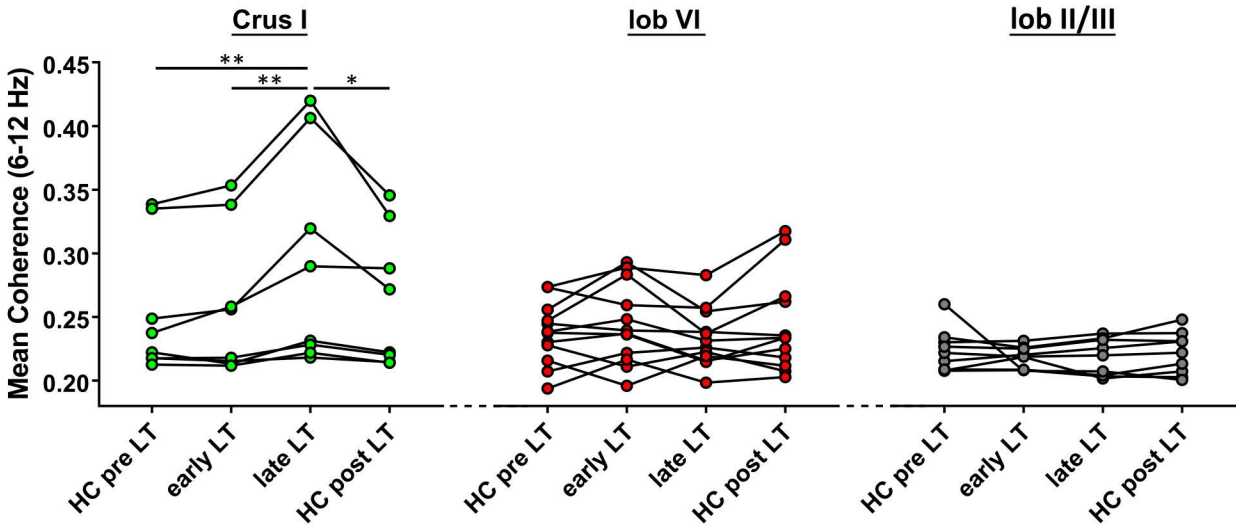
E



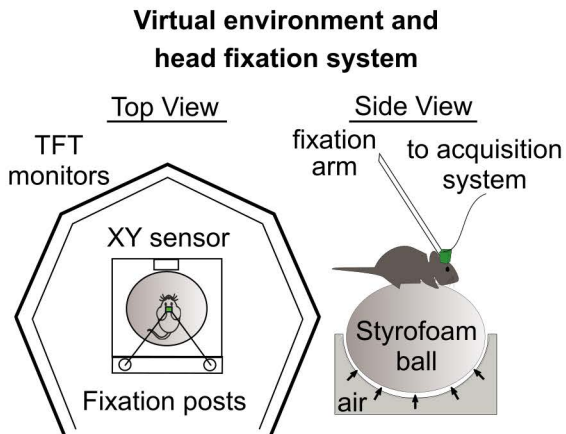
F



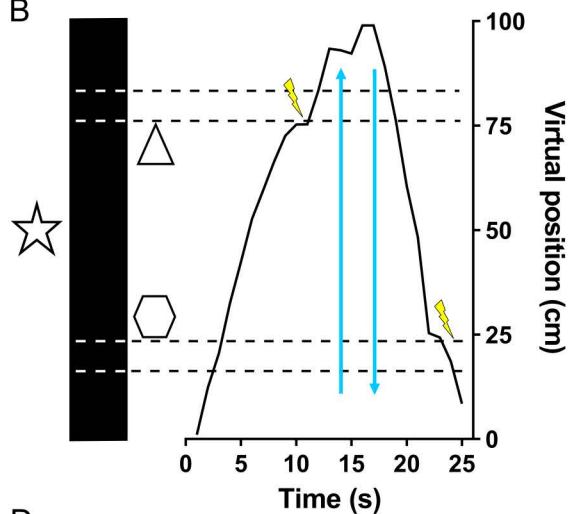




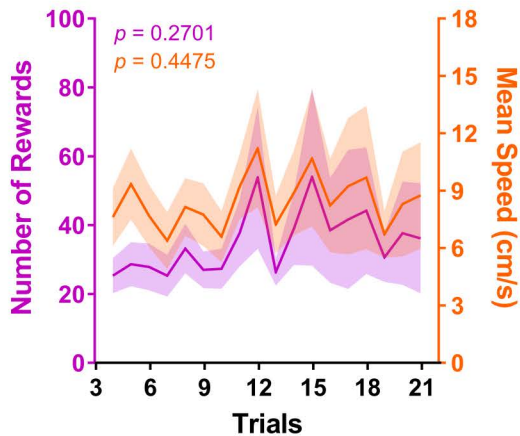
A



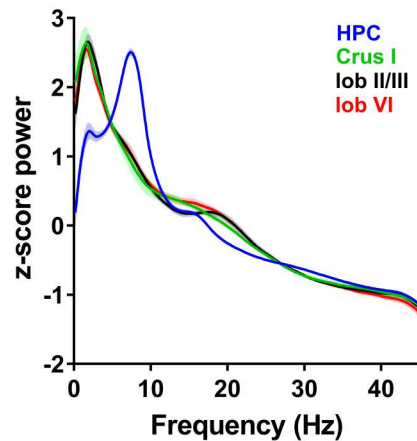
B



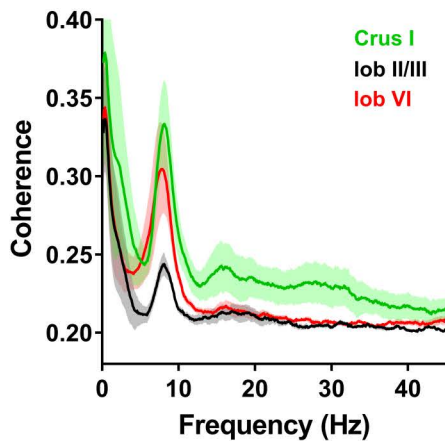
C



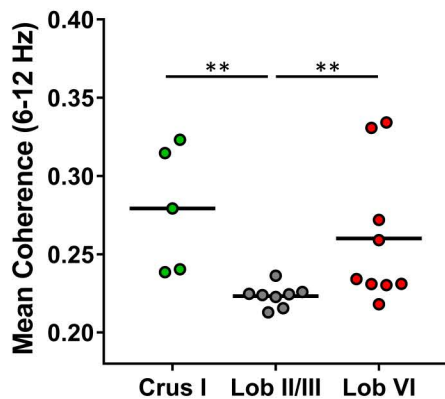
D



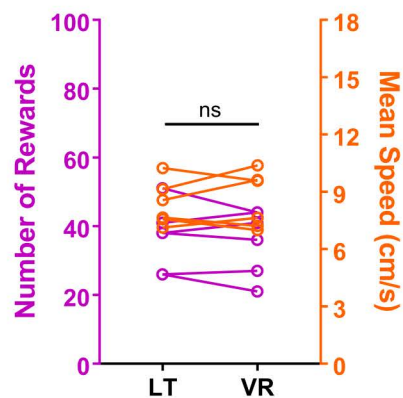
E



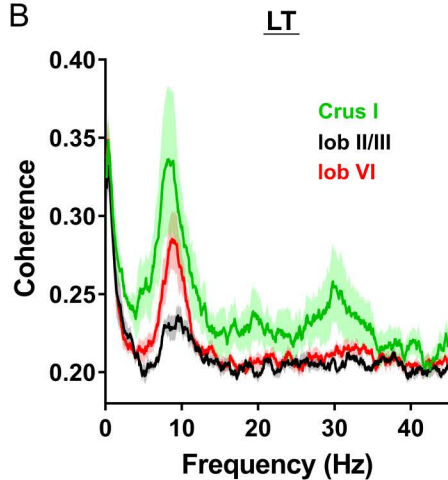
F



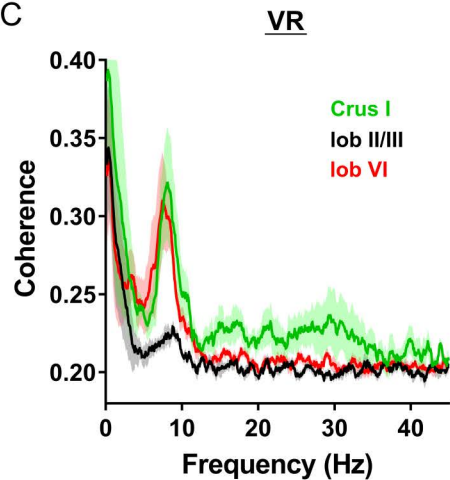
A



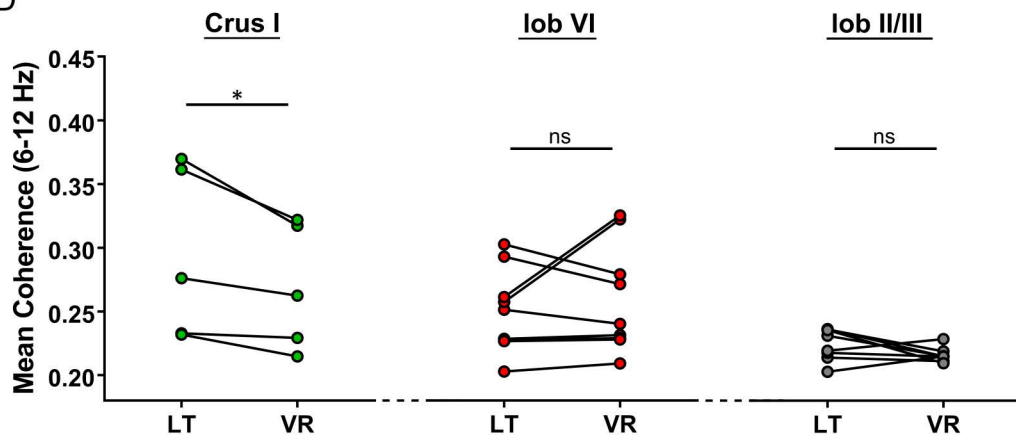
B



C



D



A**30 h**

S1

S2

S3

S4

S5

-1.46

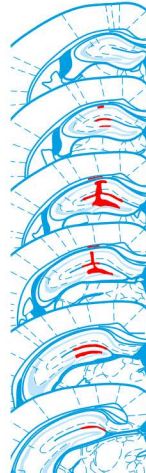
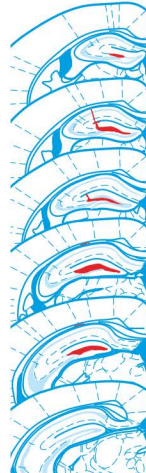
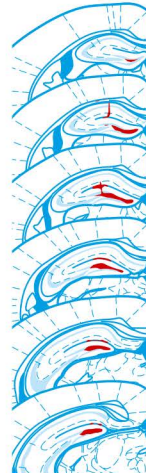
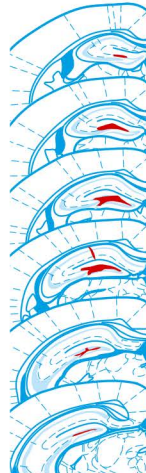
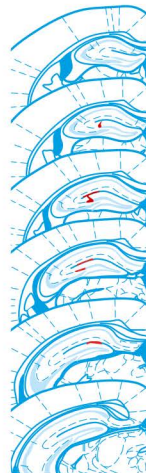
-1.70

-1.94

-2.18

-2.46

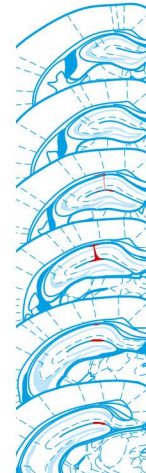
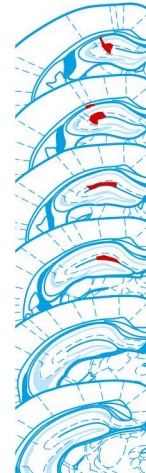
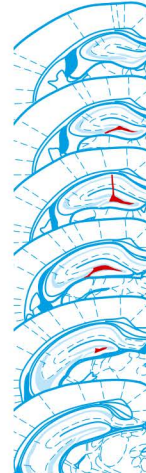
-2.70

**B****48 h**

S6

S7

S8

**C****58 h**

S9

S10

S11

S12

S13

-1.46

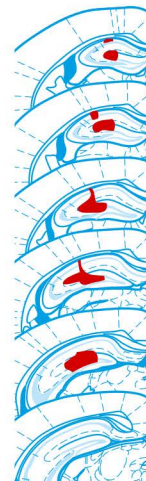
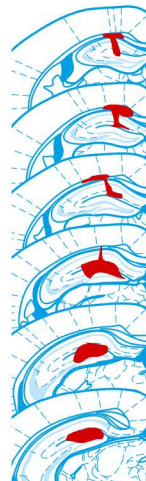
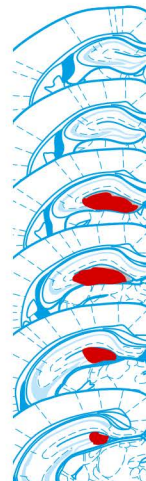
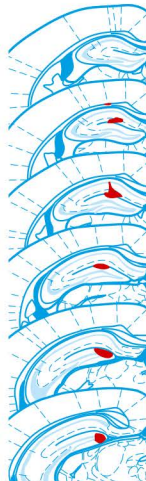
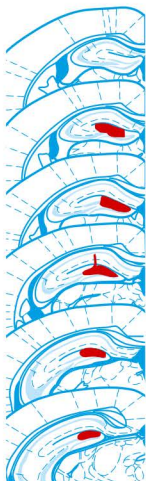
-1.70

-1.94

-2.18

-2.46

-2.70

**D****66 h**

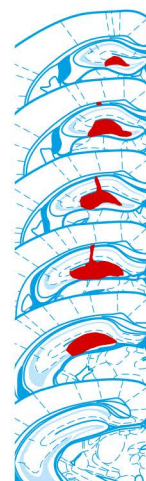
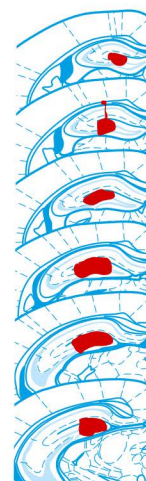
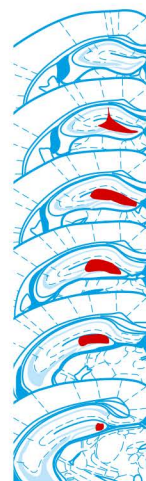
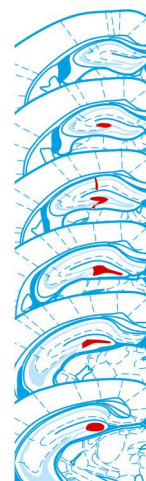
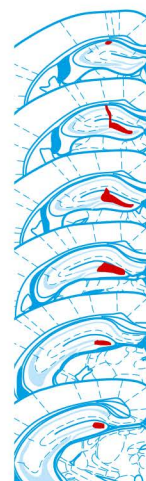
S14

S15

S16

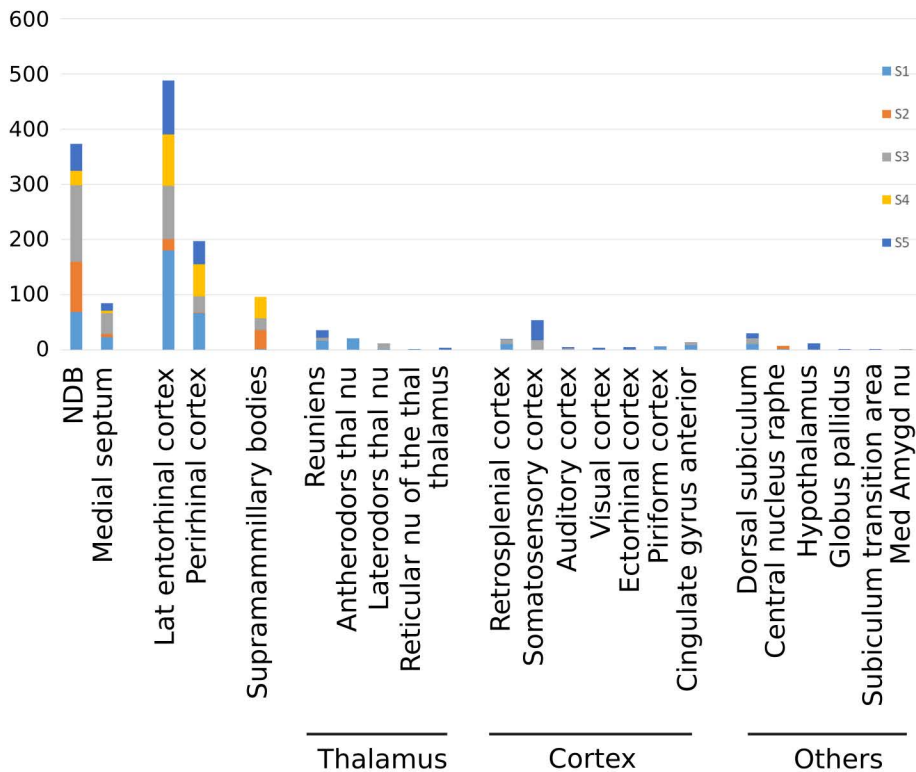
S17

S18



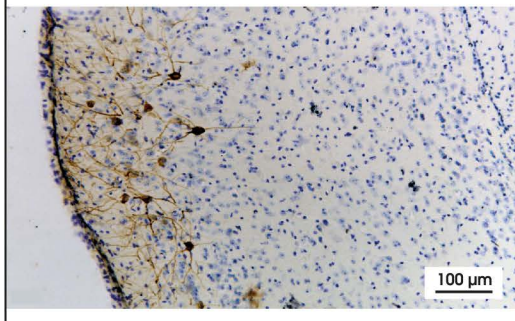
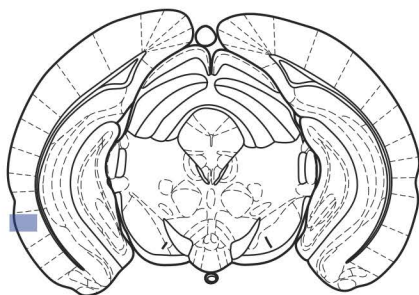
A

Sum of labeled cells per structure at 30h post rabies virus injection (n=5)



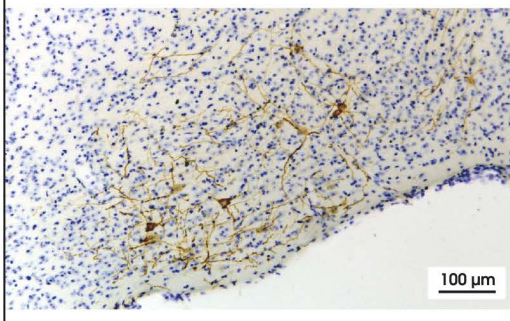
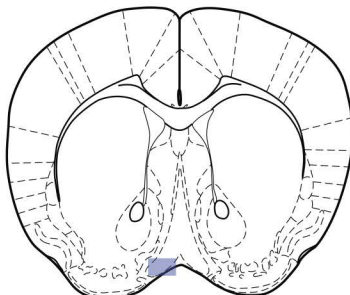
B

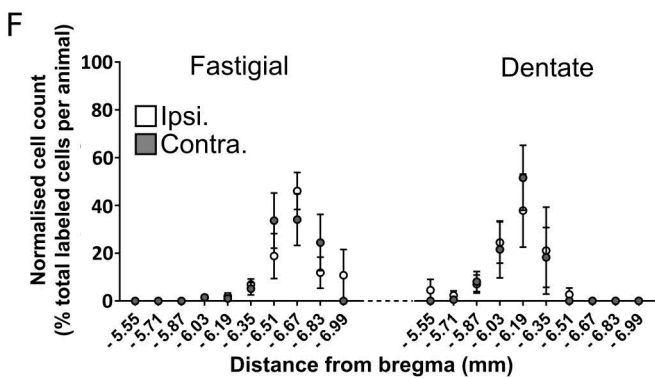
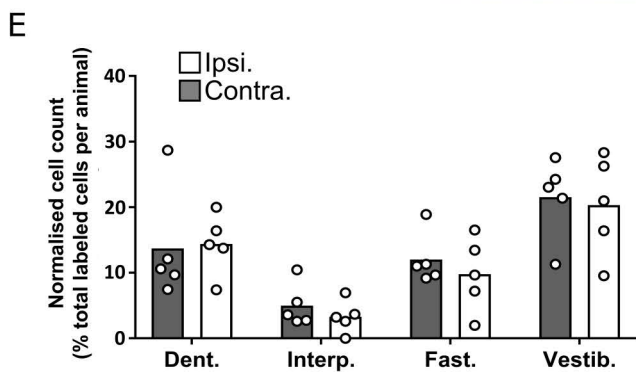
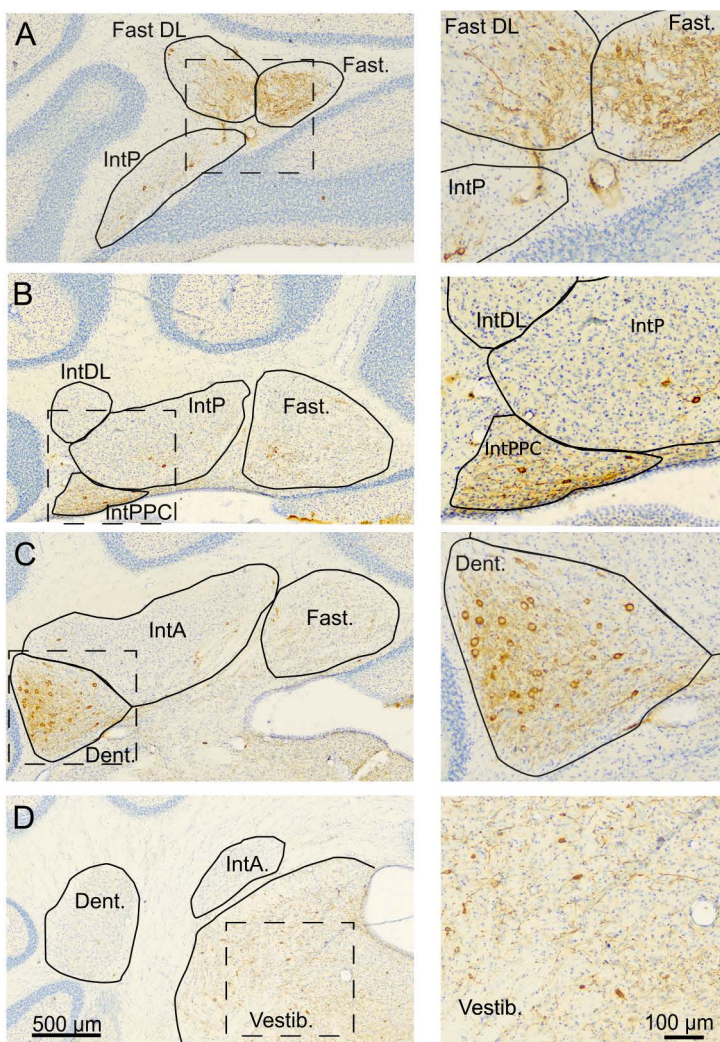
-3.64 mm



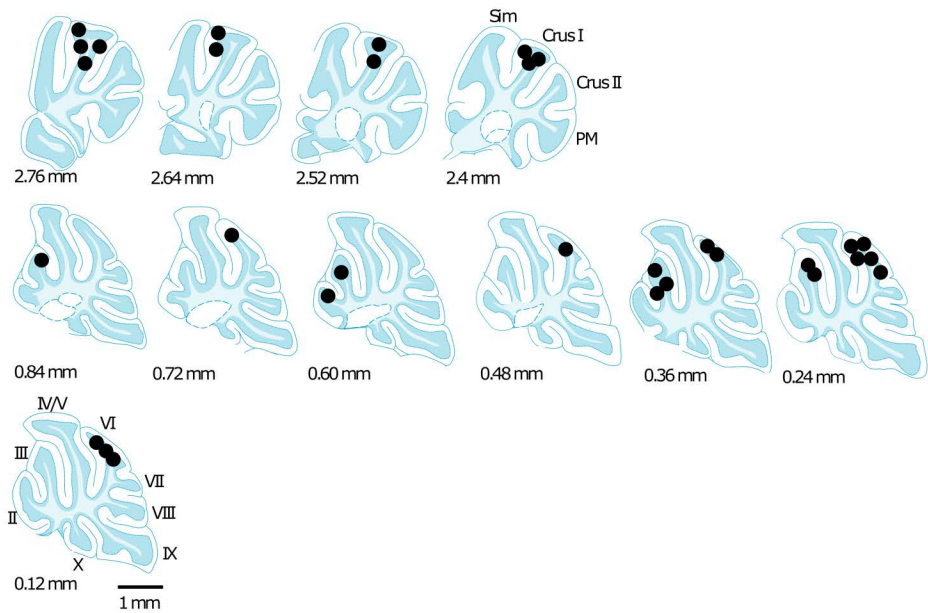
C

0.86 mm

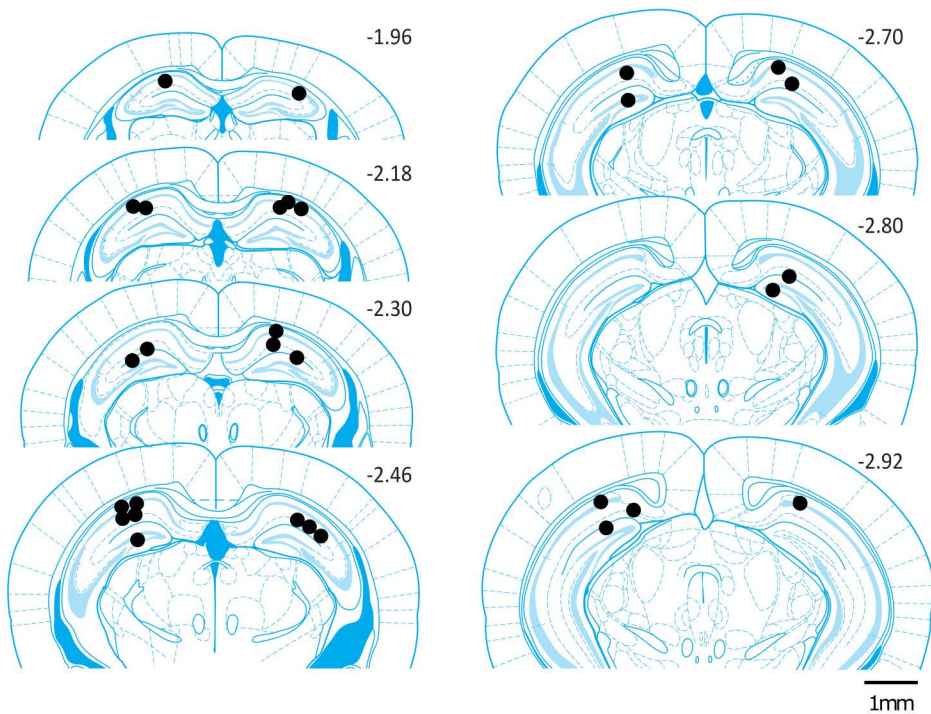




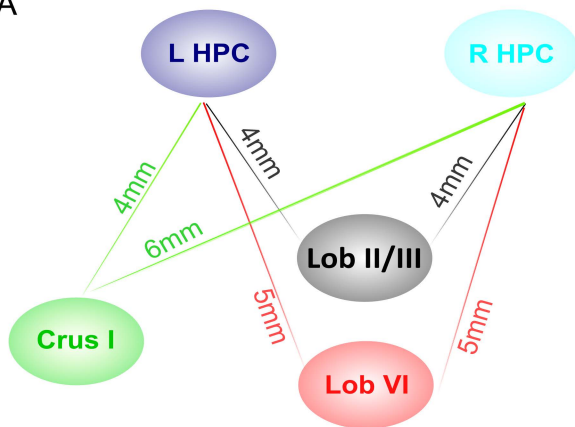
A



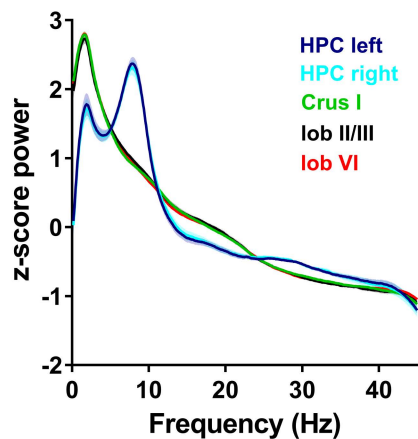
B



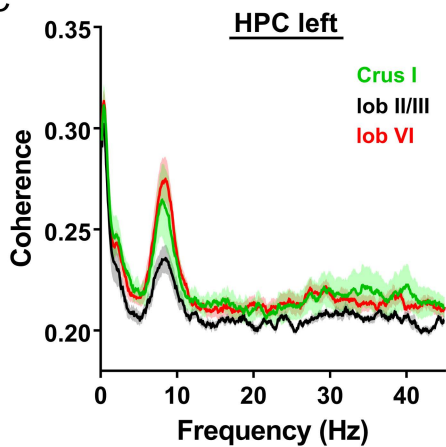
A



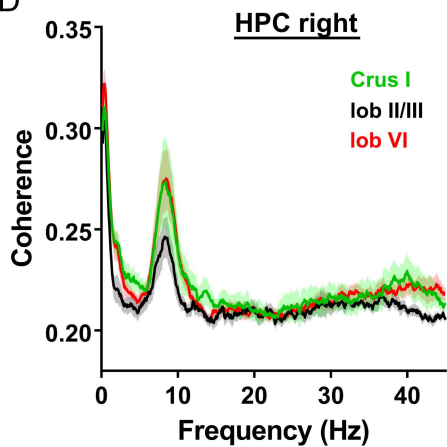
B



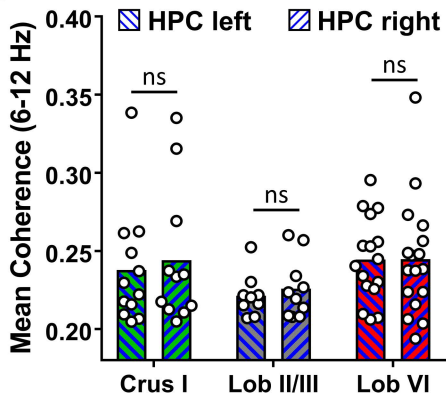
C



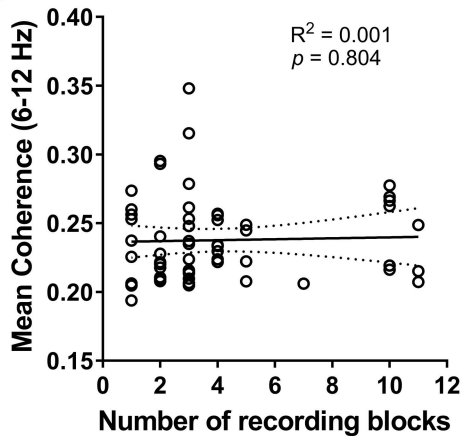
D

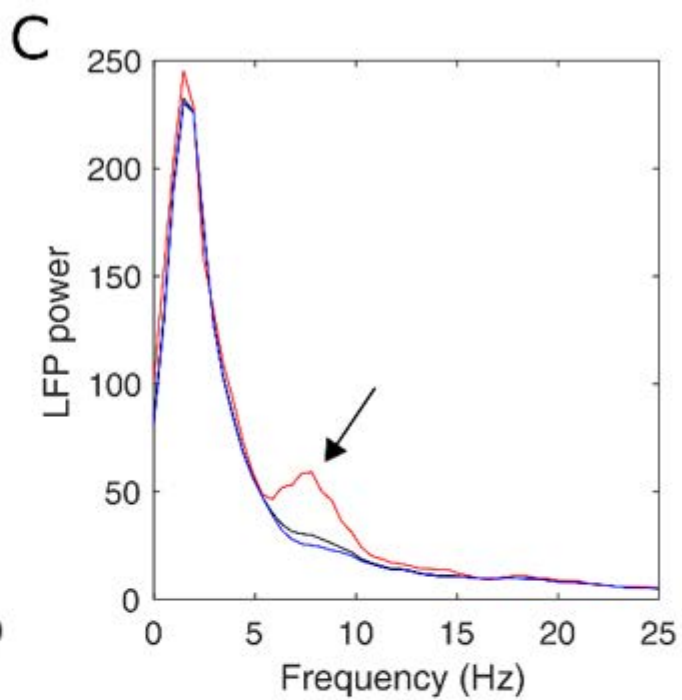
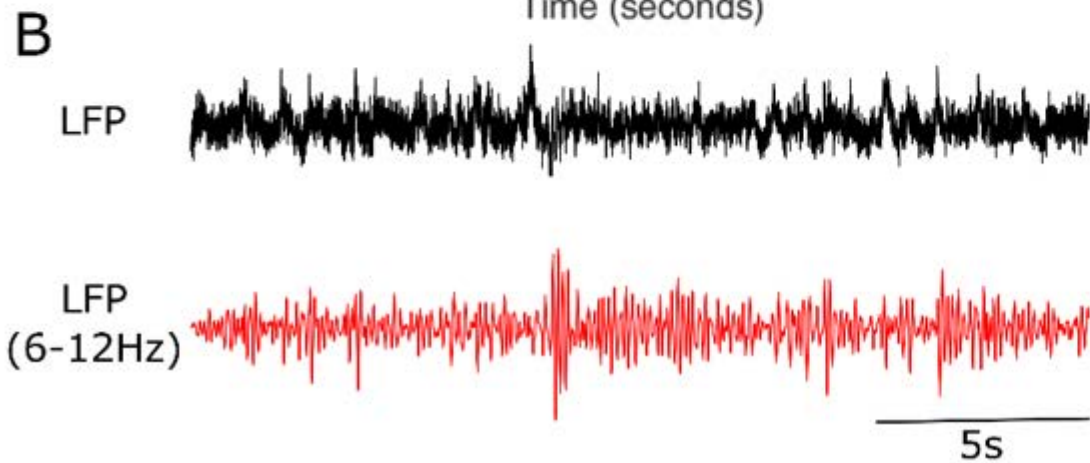
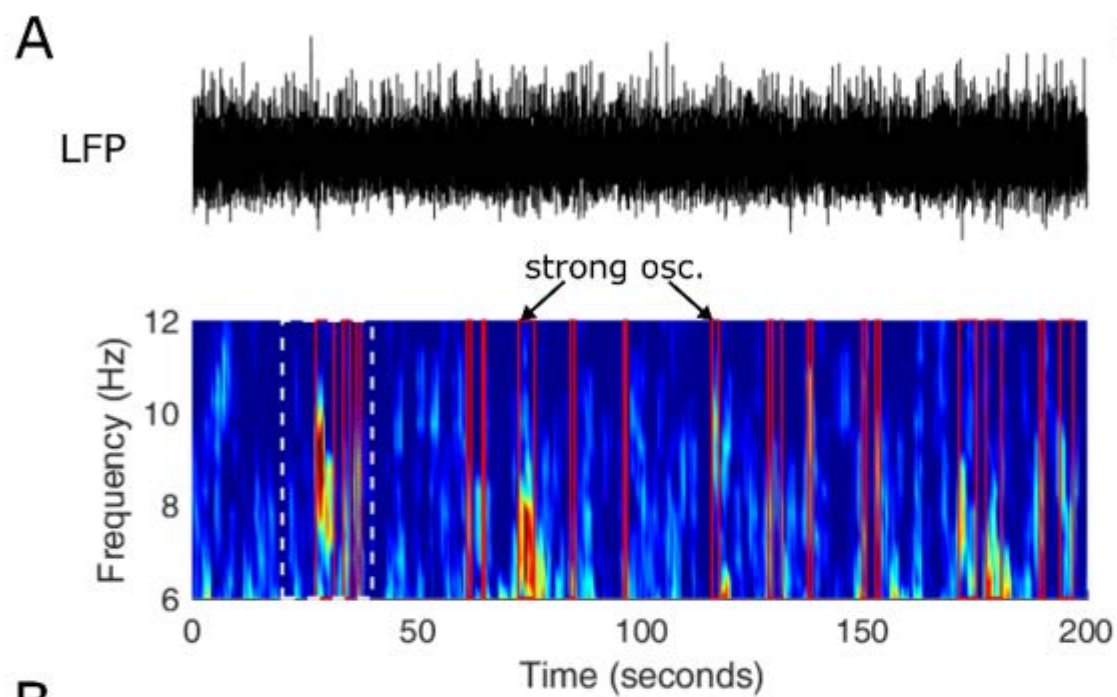


E

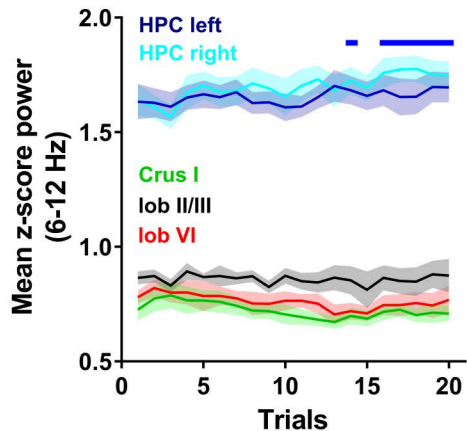


F

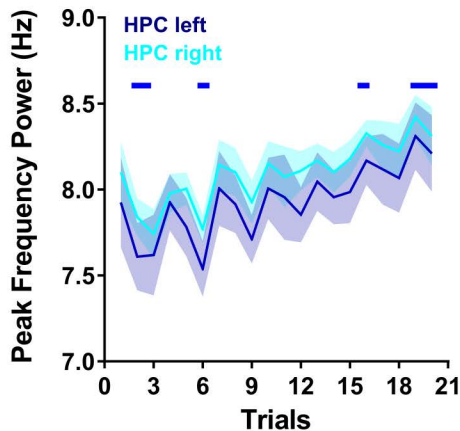




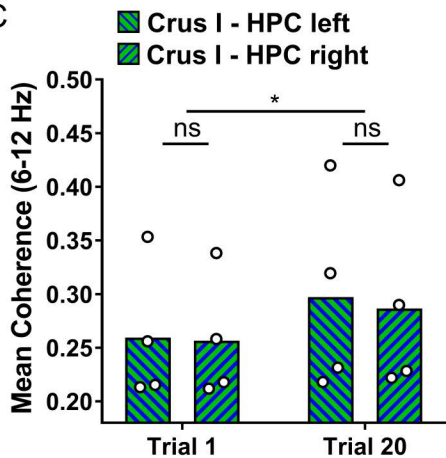
A



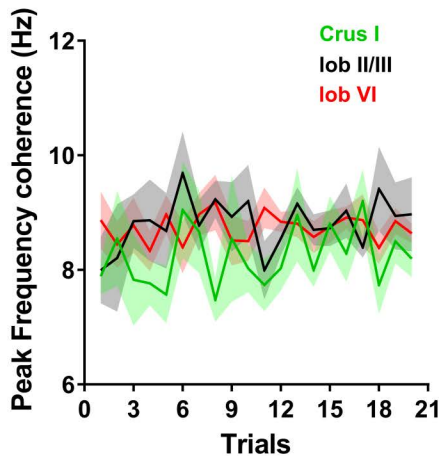
B

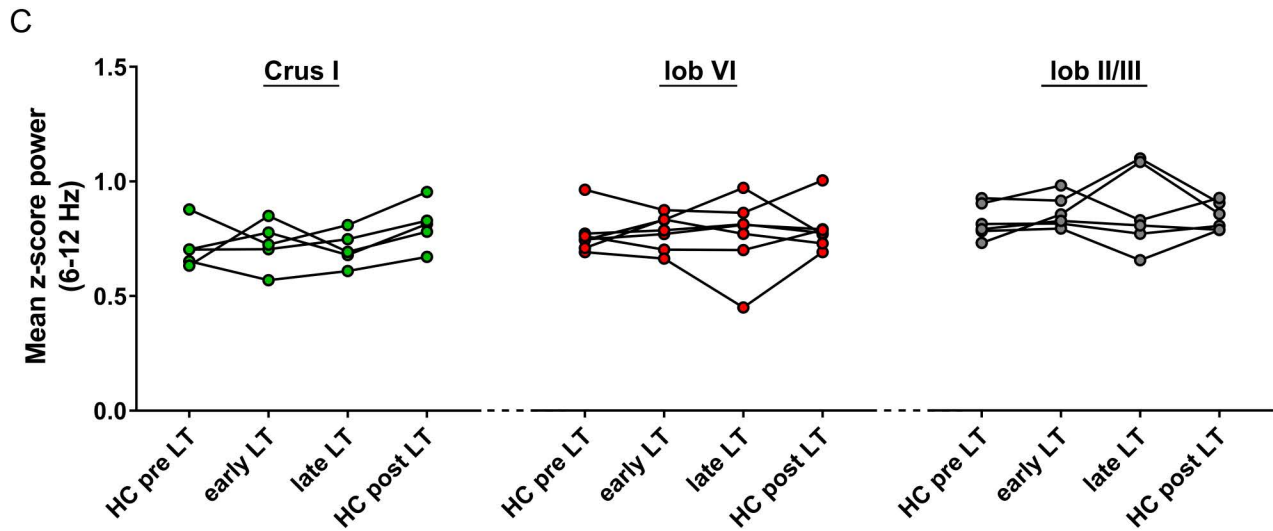
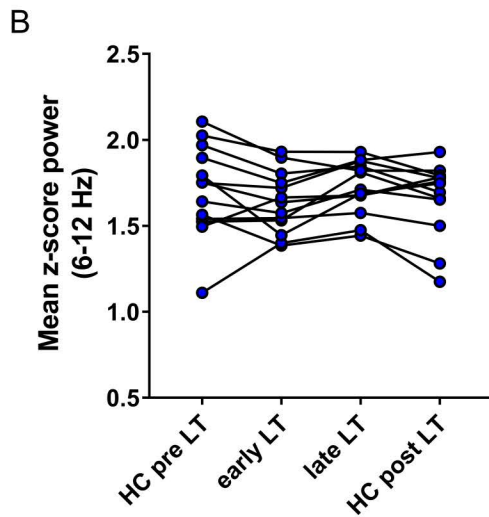
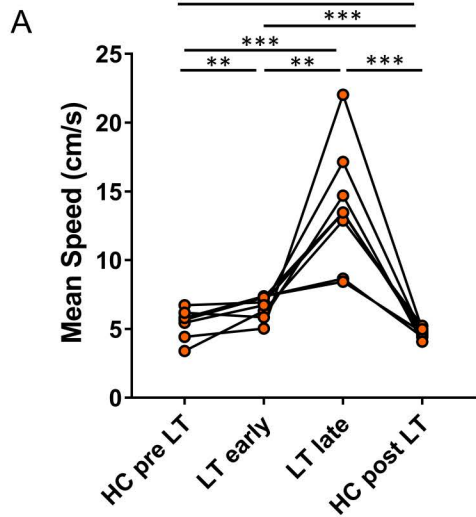


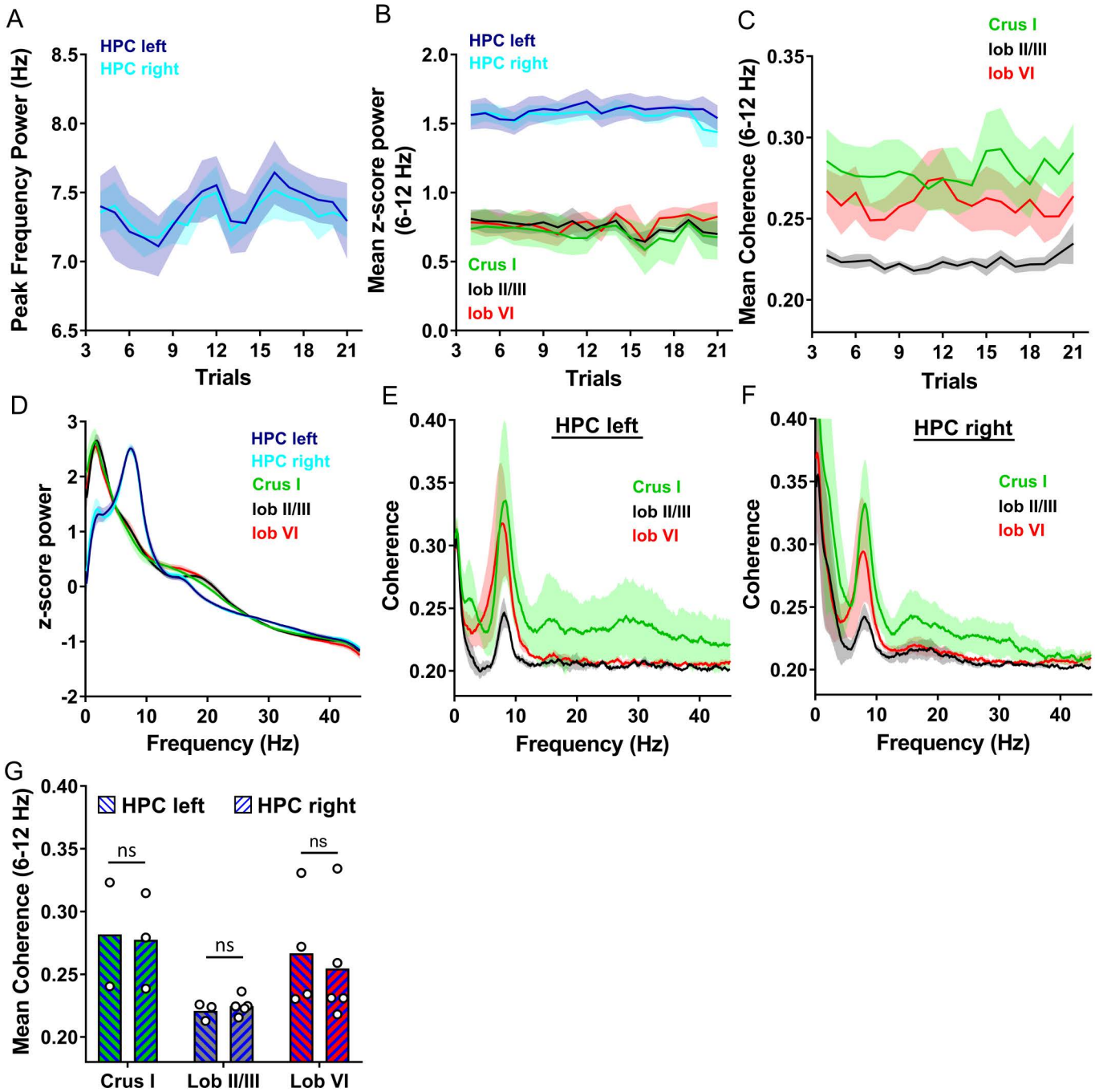
C



D







		<u>30h p.i.</u>					<u>48h p.i.</u>			<u>58h p.i.</u>					<u>66h p.i.</u>				
		S1	S2	S3	S4	S5	S6	S7	S8	S9	S10	S11	S12	S13	S14	S15	S16	S17	S18
<u>LEC</u>	i.	++	+	+++	+++	+++	++	+++	+++	+++	+++	+++	+++	+++	+++	+++	+-	+++	+++
	c.	+	-	-	+	++	-	++	++	++	++	++	++	++	++	++	++	++	++
<u>NDB/MS</u>	i.	+++	+++	+++	+++	++	+++	+++	+++	++	+++	+++	+++	+++	+++	++	+++	+++	+++
	c.	++	++	++	++	+	+++	+++	?	++	+++	+++	+++	+++	+++	++	+++	+++	+++
<u>SUM</u>	i.	-	+++	++	++	-	+++	+++	+++	++	+++	+++	+++	+++	++	+++	++	+++	+++
	c.	-	++	++	++	-	+++	+++	+++	++	+++	+++	+++	+++	++	+++	++	+++	+++
<u>Thalamus</u>		+/-	+	+	-	-	+	++	+	+	+++	++	+++	+++	+++	+++	+	++	+++
<u>Hypothalamus</u>		-	+	-	-	+	++	++	++	++	++	+++	+++	+++	+++	+++	++	+++	+++
<u>Raphe nu</u>		-	+	-	+	-	++	++	++	++	++	++	++	++	+++	+++	++	+++	+++
<u>Cortex</u>		-	-	+	-	+	++	++	++	+++	+++	+++	+++	+++	+++	+++	++	+++	+++
<u>MEC</u>	i.	-	-	-	-	-	-	+	++	+	-	++	++	++	?	+	++	++	++
	c.	-	-	-	-	-	-	+/-	+	+/-	-	+	+	+	?	+/-	+	+	+
<u>Perirhinal ctx.</u>	i.	-	-	-	-	-	-	+	+	+	+	+	+	++	++	+	++	++	
	c.	-	-	-	-	-	+	++	++	+++	+++	+++	+++	+++	+++	+++	+++	+++	+++
<u>MM</u>		-	-	-	-	-	++	++	++	++	++	++	+/-	+	++	++	+	++	++
<u>PAG</u>		-	-	-	-	-	++	++	++	++	++	+++	++	+++	+++	+++	++	+++	+++
<u>Pont. nu.</u>	i.	-	-	-	-	-	+++	+++	++	++	++	+++	+++	+++	+++	+++	+++	+++	+++
	c.	-	-	-	-	-	++	++	++	++	++	+++	+++	+++	+++	+++	+++	+++	+++
<u>Amygdala</u>	i.	-	-	-	-	-	+	+	+	+	++	++	+++	+++	++	+++	++	+++	+++
	c.	-	-	-	-	-	+	+	+	+	+++	+++	++	++	+++	+++	++	+++	+++
<u>Vestibular nu.</u>	i.	-	-	-	-	-	-	-	-	+	+	+	+	+	++	++	++	++	++ (+)
	c.	-	-	-	-	-	-	-	+/-	+	+	++	++	+	++	++	++	++	++ (+)
<u>DCN</u>	i.	-	-	-	-	-	-	-	-	+	+	+	++	++	+++	+++	+++	+++	+++
	c.	-	-	-	-	-	+/-	+/-	+/-	+	+	++	++	++	+++	+++	+++	+++	+++
<u>Cerebellar ctx.</u>	i.	-	-	-	-	-	-	-	-	-	-	+/-	+/-	+/-	++	++	++	++	++
	c.	-	-	-	-	-	-	-	-	-	-	+/-	+/-	+/-	++	++	++	++	++